

# RASCAS: Radiation SCattering in Astrophysical Simulations

L. Michel-Dansac<sup>1,\*</sup>, J. Blaizot<sup>1</sup>, T. Garel<sup>1,2</sup>, A. Verhamme<sup>2,1</sup>, T. Kimm<sup>3</sup>, M. Trebitsch<sup>4</sup>

<sup>1</sup> Univ Lyon, Univ Lyon1, Ens de Lyon, CNRS, Centre de Recherche Astrophysique de Lyon UMR5574, F-69230, Saint-Genis-Laval, France

<sup>2</sup> Observatoire de Genève, Université de Genève, 51 Ch. des Maillettes, 1290 Versoix, Switzerland

<sup>3</sup> Department of Astronomy, Yonsei University, 50 Yonsei-ro, Seodaemun-gu, Seoul 03722, Republic of Korea

<sup>4</sup> Sorbonne Université, CNRS, UMR 7095, Institut d'Astrophysique de Paris, 98 bis bd Arago, F-75014 Paris, France

Received September 15, 1996; accepted March 16, 1997

## ABSTRACT

**Context.** Resonant lines are powerful probes of the interstellar and circumgalactic medium of galaxies. Their transfer in gas being a complex process, the interpretation of their observational signatures, either in absorption or in emission, is often not straightforward. Numerical radiative transfer simulations are needed to accurately describe the travel of resonant line photons in real and in frequency space, and to produce realistic mock observations.

**Aims.** This paper introduces RASCAS, a new public 3D radiative transfer code developed to perform the propagation of any resonant line in numerical simulations of astrophysical objects. RASCAS was designed to be easily customisable and to process simulations of arbitrarily large sizes on large supercomputers.

**Methods.** RASCAS performs radiative transfer on an adaptive mesh with an octree structure using the Monte Carlo technique. RASCAS features full MPI parallelisation, domain decomposition, adaptive load-balancing, and a standard peeling algorithm to construct mock observations. The radiative transport of resonant line photons through different mixes of species (e.g. H I, Si II, Mg II, Fe II), including their interaction with dust, is implemented in a modular fashion to allow new transitions to be easily added to the code.

**Results.** RASCAS is very accurate and efficient. It shows perfect scaling up to a minimum of a thousand cores. It has been fully tested against radiative transfer problems with analytic solutions and against various test cases proposed in the literature. Although it was designed to describe accurately the many scatterings of line photons, RASCAS may also be used to propagate photons at any wavelength (e.g. stellar continuum or fluorescent lines), or to cast millions of rays to integrate the optical depths of ionising photons, making it highly versatile.

**Key words.** Methods: numerical – Radiative transfer – Galaxies: formation and evolution

## 1. Introduction

Resonant lines are very powerful tracers of the interstellar medium (ISM) and the circumgalactic medium (CGM) of galaxies: their spectral and spatial distributions imprint the kinematics and the geometry of the gas in which they scatter. The Lyman- $\alpha$  line of hydrogen is the brightest resonant line, extensively used to observe statistical samples of galaxies (e.g. Ouchi et al. 2008, 2010; Sobral et al. 2017; Drake et al. 2017; Hashimoto et al. 2017; Itoh et al. 2018; Herenz et al. 2019), from the local Universe (Hayes et al. 2013; Henry et al. 2015; Yang et al. 2017; Verhamme et al. 2017) to the highest redshifts (e.g. Zitrin et al. 2015; Stark et al. 2017).

Other lines, now also commonly detected in the spectra of galaxies, contain the same richness of information as Lyman- $\alpha$  does. In the near-ultraviolet domain the Mg II  $\lambda\lambda 2796, 2804$  resonant doublet is one of the brightest. At low redshift it has been compared to Lyman- $\alpha$  for a small sample of Green Pea galaxies (Henry et al. 2018). At intermediate redshift it has been recently observed in MUSE-selected galaxies (Finley et al. 2017b; Feltre et al. 2018), and has been compared to Fe II ( $\lambda\lambda 2365, \lambda\lambda 2396, \lambda\lambda 2612, \lambda\lambda 2626$ , Finley et al. 2017b). In addition, the first Fe II\* extended emission has been reported (Finley et al. 2017a).

In the far-ultraviolet domain, C II  $\lambda 1335$  and several Si II lines ( $\lambda\lambda 1190, \lambda\lambda 1193, \lambda\lambda 1194, \lambda\lambda 1197$ ) are commonly detected in the spectra of galaxies (Shapley et al. 2003; Zhu et al. 2015; Trainor et al. 2015; Rivera-Thorsen et al. 2015; Chisholm et al. 2017). Higher energy transitions are also resonant, such as Si IV  $\lambda\lambda 1394, 1403$  and C IV  $\lambda\lambda 1548, 1551$ , probing a hotter phase of the ISM and CGM of galaxies. With the advent of sensitive instruments such as the MUSE Integral Field Spectrograph on the Very Large Telescope (VLT, Bacon et al. 2010), resonant line observations hold great potential in revealing the chemical enrichment of the intergalactic medium (IGM) by galaxies, the kinematics of the CGM, and the interplay between the infall and outflow of gas around galaxies. However, resonant lines are not straightforward to interpret. Realistic radiative transfer simulations are needed to retrieve all information from the data.

Numerical simulations have become an indispensable tool to understand galaxy formation. The continuous progress both in numerical simulation algorithms and in the supercomputer platforms themselves is such that we are today able to compute simulations of galaxies which embrace the full complexity of their large-scale cosmological environment while resolving the details of the ISM, and to include increasing levels of physics, such as the coupling of ionising radiation or magnetic fields with gas (e.g. Rosdahl et al. 2018; Martin-Alvarez et al. 2018).

In order to assess the success of a simulation and the validity of the many assumptions that went into it, it is necessary to com-

\* e-mail: leo.michel-dansac@univ-lyon1.fr

pare the results with observations. This is generally not an obvious thing to do, as simulation predictions are physical properties (e.g. density, temperature, velocities), while observations collect photons in various forms (spectra, images, cubes) which originate from different processes (e.g. stellar emission, nebular emission, fluorescence) and have possibly been altered on their way to the telescope (e.g. scattering, absorption by dust, IGM transmission, instrumental effects). The maturity and high resolution (less than a few 10pc) of the current state-of-the-art simulations offer the opportunity to produce mock observations that account for these processes with the necessary accuracy. In turn, provided the simulations represent the Universe with a high enough degree of realism, these mock observations are extremely useful for the interpretation of observations or to test and/or predict observational diagnostics. First, they are necessary to interpret complex observations within a robust theoretical framework. An example here is the interpretation of diffuse Lyman- $\alpha$  emission seen in deep narrow-band stacks (e.g. Steidel et al. 2011; Momose et al. 2014) or in VLT/MUSE data-cubes (Wisotzki et al. 2016; Leclercq et al. 2017) in relation with the multi-band photometry from *Hubble* Space Telescope (HST). The interpretation of these phenomena requires self-consistent multi-wavelength mocks that include the full radiative transfer (RT) effects due to Lyman- $\alpha$  scattering and dust extinction. Another example is the very difficult interpretation of absorption lines in galaxy spectra because observations cannot tell us whether they are due to the ISM or CGM. Second, mock observations are very useful to prepare and optimise observational strategies for forthcoming surveys. Similarly, mocks are often used before the instruments are operational as example scenes which help validate data reduction and data analysis pipelines. Third, mock observations may be used to validate the accuracy with which physical properties (e.g. stellar mass, star formation rate) are inferred from observations, since these are known quantities from the simulations.

This paper presents a new 3D RT code, RAdiation SCattering in Astrophysical Simulations (RASCAS), which was designed to construct accurate multi-wavelength mock observations (spectra, images, or datacubes) from high-resolution simulations. RASCAS deploys a general two-step methodology (e.g. Hummels et al. 2017; Barrow et al. 2017). The first step consists in extracting all relevant information from the simulation outputs: (1) the information concerning the medium through which light will propagate, and (2) the information concerning the sources of radiation. Point (1), for example, determines the number density of H I atoms, their thermal velocity dispersion and bulk velocity, and the dust density, everywhere in a chosen volume. Fully coupled radiation-hydrodynamic simulations would naturally provide the information about ionised states, but retrieving this information in pure hydrodynamic simulations may be tricky. In such case, it is necessary to process the simulation outputs with additional software and models, typically with CLOUDY (Ferland et al. 2013), as in Hummels et al. (2017) and Barrow et al. (2017), or with independent codes which solve for H and He ionisation by propagating ionising radiation in post-processing (e.g. Li et al. 2008; Yajima et al. 2012). Point (2) is also involved to a greater or lesser extent, depending on the sources. Computing the continuum emission from star particles is relatively straightforward, using spectro-photometric models of stellar populations (e.g. Bruzual & Charlot 2003; Eldridge et al. 2017). However, computing the emission lines from the gas (e.g. in the Lyman- $\alpha$  line or in other nebular lines) again requires a detailed knowledge of the ionisation and thermal state of the emitting species. This may be provided by the simulation code, as is the case for H and He with RAMSES-RT (Rosdahl et al. 2013), or it may be

necessary to post-process the simulation to estimate the emissivities of the gas. This first step is very simulation- and model-dependent, and RASCAS chooses to encapsulate it in a simulation-plugin module and to implement two stand-alone pre-processing codes which generate an adaptive mesh with all the needed physical information about the gaseous medium, and the initial conditions for light emission in the form of lists of photon packets. These datasets, which could easily be generated from other simulations with any post-processing code, serve as inputs to RASCAS to perform the radiative transfer computation.

The core of RASCAS, is then the second step, which is passive radiative transfer, passive in the sense that radiation does not affect the properties of the gas. Here RASCAS inherits directly from the code McLYA (Verhamme et al. 2006, 2012; Trebitsch et al. 2016) and joins the now long tradition of Monte Carlo codes which compute the resonant scattering of Lyman- $\alpha$  photons through simulations (Cantalupo et al. 2005; Tasitsiomi 2006; Semelin et al. 2007; Laursen et al. 2009a; Pierleoni et al. 2009; Kollmeier et al. 2010; Zheng et al. 2010; Laursen et al. 2011; Yajima et al. 2012; Behrens & Niemeyer 2013; Smith et al. 2015; Gronke & Bird 2017; Abe et al. 2018) or through idealised configurations (Ahn et al. 2001; Zheng & Miralda-Escudé 2002; Dijkstra et al. 2006; Hansen & Oh 2006; Barnes & Haehnelt 2010; Forero-Romero et al. 2011; Orsi et al. 2012; Lake et al. 2015; Gronke & Dijkstra 2016; Eide et al. 2018). The novelty of RASCAS compared to these Lyman- $\alpha$  RT codes is a combination of the following qualities: (1) RASCAS is a public code and, being the latest implementation, incorporates a selection of state-of-the-art algorithms presented in other codes; (2) RASCAS is designed in a very modular way and can be used for Lyman- $\alpha$  RT, but also for computing radiative transfer of any other resonant (or not) line and continuum radiation (with arbitrary spectral shapes); (3) RASCAS is massively parallel and implements a domain decomposition which allows it to run with a negligible memory footprint on many cores, thus making it a perfect tool to process extremely large simulations on very large supercomputers.

The layout of the paper follows the Monte Carlo workflow. In Sect. 2 we describe how we sample radiation sources with photon packets. In Sect. 3 we present our methods for solving radiative transfer in a single simulation cell. In Sect. 4 we detail our parallel implementation on adaptive grids with domain decomposition. We then present brief illustration for possible applications in Sect. 5 and sum up in Sect. 6.

## 2. Emission of photon packets

In this section, we describe how we generate photon packets from various sources of radiation. In doing so, we sample the spectral and angular distributions which characterise each source with a number of photon packets that relates to the luminosities of the sources. In the current implementation, all sources considered (star particles or gas cells) are isotropic, and photon packets are emitted with random directions. Anisotropic sources may be useful, for example to describe an active galactic nucleus or to set up idealised experiments with specific illuminations (e.g. plane-parallel, beam). The framework of RASCAS makes this trivial. RASCAS also gives an equal weight to all photon packets so that they are cast from different sources with a probability  $P = \dot{N}_\gamma / \dot{N}_\gamma^{\text{tot}}$ , where  $\dot{N}_\gamma$  is the number of (real) photons emitted by a source per unit time and  $\dot{N}_\gamma^{\text{tot}}$  the sum of  $\dot{N}_\gamma$  over all sources. We detail below how we compute these terms in different configurations.

In the framework of RASCAS, this first step is done by a stand-alone code which generates a simple photon packet initial con-

dition (PPIC) file for each experiment. This file contains a list of photon packets, each with an ID, a position, a direction, and a frequency. These PPIC files are then fed to RASCAS, which propagates each photon packet regardless of the sources. This very flexible approach is possible because the radiative transfer done with RASCAS is passive (i.e. it does not change the properties of the gas). It allows statistics to be added incrementally by regenerating additional PPIC files on demand, and it makes it very easy to combine different signals (e.g. stellar continuum and nebular lines) run as separate experiments. The simplicity of these PPIC files also renders trivial the generation of any ad hoc source model.

Three stand-alone codes are currently available to generate PPIC files for different sources. These codes, which may serve as templates for future developments by interested users, are described in the following subsections.

### 2.1. Emission from stars

The first stand-alone code, `PhotonsFromStars`, generates photon packets from star particles which represent stellar populations of single ages and metallicities. Four spectral shapes are implemented: (1) a power-law fit to the stellar continuum, (2) a tabulated version of the stellar continuum, (3) a Gaussian emission line, and (4) a monochromatic line. In all cases, the stellar emissivity from star particles is computed with a 2D interpolation in age and metallicity of tabulated spectro-photometric models such as Bruzual & Charlot (2003) or Eldridge et al. (2017).

The frequencies of photon packets are defined in the rest frames of the sources and then shifted to an external frame according to each source's velocity. We give details below for the different spectral shapes.

#### Power-law continuum

Here we consider a continuum flux density described by a power law  $F_\lambda = F_0(\lambda/\lambda_0)^\beta$  between two boundaries  $\lambda_{\min}$  and  $\lambda_{\max}$ . Both  $F_0$  and  $\beta$  depend on age and metallicity and are different for each star particle. The number of photons emitted per unit time by this continuum is

$$\dot{N}_\gamma = \begin{cases} \frac{F_0(\lambda_{\max}^{\beta+2} - \lambda_{\min}^{\beta+2})}{hc\lambda_0^{\beta+2}} & \text{if } \beta \neq -2, \\ \frac{F_0\lambda_0^2}{hc} \ln(\lambda_{\max}/\lambda_{\min}) & \text{if } \beta = -2, \end{cases} \quad (1)$$

and each source will emit on average  $N_{\text{MC}} \times \dot{N}_\gamma / \dot{N}_\gamma^{\text{tot}}$  photon packets, where  $N_{\text{MC}}$  is the total number of photon packets generated. In practice, once  $\dot{N}_\gamma$  is known for all sources, we store the normalised cumulative luminosity distribution of sources into an array  $P$ , so that the  $i$ -th element of the array,  $P_i$ , has a value equal to the probability of emission by a particle with index  $\leq i$ . Then, for each photon packet, we draw a univariate  $r$  between 0 and 1, and locate  $r$  in the array  $P$  with a bi-section algorithm so that  $P_{i-1} < r \leq P_i$ . This gives us the index  $i$  of the star particle which will emit the photon packet.

When a star particle emits a photon packet, we derive a wavelength by sampling the photon number distribution  $P(\lambda) = \lambda F_\lambda \dot{N}_\gamma / hc$ . This function is integrable analytically, so that the probability of emitting a photon with wavelength in  $[\lambda_{\min}; \lambda]$  is written  $P(< \lambda) = (\lambda^{2+\beta} - \lambda_{\min}^{2+\beta}) / (\lambda_{\max}^{2+\beta} - \lambda_{\min}^{2+\beta})$  for  $\beta \neq -2$ , and  $P(< \lambda) = \ln(\lambda/\lambda_{\min}) / \ln(\lambda_{\max}/\lambda_{\min})$  for  $\beta = -2$ . These two expressions can be inverted, and we simply need to draw a univariate  $r$  between 0 and 1 to compute the wavelength  $\lambda$  of the photon

packet as

$$\lambda = \begin{cases} \left[ \lambda_{\min}^{2+\beta} + r \times (\lambda_{\max}^{2+\beta} - \lambda_{\min}^{2+\beta}) \right]^{1/(2+\beta)} & \text{if } \beta \neq -2, \\ \lambda_{\min} \times e^{r \ln(\lambda_{\max}/\lambda_{\min})} & \text{if } \beta = -2. \end{cases} \quad (2)$$

#### Tabulated continuum from stellar populations

To obtain more realistic spectra including, for example, stellar atmosphere absorption features, we follow the same strategy as above with small modifications. We replace Eq. 1 with numerical estimates computed directly from the tabulated spectra provided by spectro-photometric libraries, using a linear interpolation of  $F_\lambda$  in wavelength. As above, this first step allows us to assign photon packets to sources as a function of their ages and metallicities. Then, in order to define the wavelength of a photon packet, we store in an array  $P$  the normalised cumulative number of photons (per unit time) emitted by its source between  $\lambda_{\min}$  and  $\lambda_i$ , where  $\lambda_i$  are the values at which the library provides  $F_\lambda$  values. Drawing one univariate allows us, with a strategy similar to that above, to locate the wavelength bin in which the photon packet is emitted. Once this is known, we keep following the procedure by drawing a second univariate to compute the wavelength of the photon packet using Eq. 2 where the power law is now linear and describes  $F_\lambda$  in the range  $[\lambda_{i-1}; \lambda_i]$ . This method produces a linearly interpolated version of the input tabulated energy distribution.

#### Gaussian line

In some experiments the aim might be to model the emission lines from star particles, for example as a proxy for nebular emission from H II regions (e.g. Verhamme et al. 2012; Behrens & Braun 2014). In such cases,  $\dot{N}_\gamma$  is the number of photons emitted per second in the line, and can be derived from the number of ionising photons emitted by each star particle as a function of its age and metallicity. We follow here the same strategy as above, with normalisation factors which depend on the nebular line under consideration, and assign a source for each photon packet.

In order for frequencies of photon packets to be distributed along a Gaussian centred on frequency  $\nu_0$  and of standard deviation  $\sigma_\nu$ , we use the Box-Muller method: we draw two random numbers  $r_1$  and  $r_2$  uniformly distributed between 0 and 1 and compute  $\nu = \nu_0(1 + \sqrt{-2 \ln(r_1)} \cos(2\pi r_2) \sigma_\nu)$ . We note that this implementation makes the approximation that photons have the same energy across the line (in the frame of each source). This is generally acceptable for lines broadened by a characteristic velocity  $v \ll c$ , with an error in  $v/c$ .

#### Monochromatic line

A final case of interest is monochromatic emission from star particles. This may be used for at least two purposes: (1) a simplification of line emission and (2) a way to obtain a quick estimate of the continuum flux at any wavelength. In case (1) the same procedure as Gaussian emission is followed, but the frequency of all photon packets are the same (in the frame of each source). In (2) the emitted number of photons per unit time is used at the chosen wavelength  $\lambda_{\text{em}}$ ,  $\dot{N}_\gamma = \lambda_{\text{em}} F_\lambda(\lambda_{\text{em}}/hc)$ , to assign sources to photon packets, and again the frequencies of all photon packets are the same.

## 2.2. Lyman- $\alpha$ emission from gas

The second stand-alone code, `LyaPhotonsFromGas`, generates photon packets which describe Lyman- $\alpha$  emission from the gas<sup>1</sup>. This code was written to exploit `RAMSES-RT` simulations, where the ionisation state of hydrogen is known, so that Lyman- $\alpha$  emission can be computed directly from the simulation outputs. We note that there are two contributions to Lyman- $\alpha$  emission: recombinations and collisions. We treat the two separately, and generate an independent PPIC file for each.

This time the sources are adaptive mesh refinement (AMR) cells, not particles, and we assume that emission is homogeneous within each cell. We follow a similar strategy to that for star particles, and first we compute the number of Lyman- $\alpha$  photons emitted per unit time by each cell. For recombinations, we assume the case B conditions and, following Cantalupo et al. (2008), we compute the number of Lyman- $\alpha$  photon emitted per unit time from each cell as

$$\dot{N}_{\gamma,\text{rec}} = n_e n_p \epsilon_{\text{Ly}\alpha}^{\text{B}}(T) \alpha_{\text{B}}(T) \times (\Delta x)^3, \quad (3)$$

where  $n_e$  and  $n_p$  are the electron and proton number densities, predicted by our simulation as a function of the local radiation field and read directly from `RAMSES-RT` outputs;  $\alpha_{\text{B}}(T)$  is the case B recombination coefficient;  $\epsilon_{\text{Ly}\alpha}^{\text{B}}(T)$  is the fraction of recombinations producing Lyman- $\alpha$  photons; and  $(\Delta x)^3$  is the volume of the cell. We evaluate  $\epsilon_{\text{Ly}\alpha}^{\text{B}}(T)$  with the fit from Cantalupo et al. (2008, their Eq. 2), and  $\alpha_{\text{B}}(T)$  with the fit from Hui & Gnedin (1997, their appendix A). For the collisional term, we compute the number of Lyman- $\alpha$  photons emitted per unit time from each cell as

$$\dot{N}_{\gamma,\text{col}} = n_e n_{\text{H I}} C_{\text{Ly}\alpha}(T) \times (\Delta x)^3, \quad (4)$$

where  $n_{\text{H I}}$  is the number density of neutral hydrogen atoms, read directly from the simulation outputs, and  $C_{\text{Ly}\alpha}(T)$  is the rate of collisional excitations from level  $1s$  to level  $2p$  which we evaluate with the fit from Goerdt et al. (2010, their Eq. 10). Once these luminosities are known for all cells, we use the same algorithm as for star particles to assign photon packets to cells.

Finally, for each photon packet, we generate random emission coordinates within its emission cell, and compute an emission wavelength in the frame of the cell following the Gaussian line method outlined for star particles. In this case, we relate the width of the Gaussian to the mean velocity of hydrogen atoms through  $\sigma_v = v_0(2k_B T/m_p)^{1/2}/c$ , where  $k_B$  is Boltzmann's constant and  $m_H$  the mass of a hydrogen atom.

## 2.3. Ad hoc source models

The simplicity of PPIC files makes it straightforward to write these files with any idealised configuration. A few examples are implemented in the `RASCAS` distribution, which can be used as they are or extended to different configurations.

## 3. Radiative transfer in a homogeneous medium

In this section we discuss the implementation of Monte Carlo radiative transfer (MCRT) through a homogeneous medium (e.g. a simulation cell). Unless mentioned otherwise, we compute frequencies and velocities in the frame of that medium. Extending this to the general case is simply a matter of representing

<sup>1</sup> This code can be easily customised to deal with any other emission line from the gas.

a complex gas distribution on a grid (see Sect. 4) and dealing with changes of frames from cell to cell. To the first order in  $(v_g/c)$ , where  $\mathbf{v}_g$  is the velocity of the gas relative to some external frame, the frequency of a photon packet in the gas frame  $\nu$  can be related to that in the external frame  $\nu_{\text{ext}}$  with  $\nu_{\text{ext}} = \nu(1 + (\mathbf{k} \cdot \mathbf{v}_g)/c)$ , where  $\mathbf{k}$  is the propagation direction vector.

Photon packets propagate along straight lines between interactions with matter or until they escape the computational domain towards the observer. After emission, or after each scattering, the optical depth to the next scattering event is drawn from an exponential distribution using

$$\tau_{\text{event}} = -\ln(r), \quad (5)$$

where  $r$  is a uniformly distributed random number. The photon packet is advanced in space until the optical depth  $\tau$  it covered reaches  $\tau_{\text{event}}$ , at which point the interaction occurs. In practice, we propagate photon packets through a grid, and they may have to cross more than one cell before reaching  $\tau_{\text{event}}$ . In such cases, photon packets are moved from cell to cell, each time subtracting to  $\tau_{\text{event}}$  the contribution  $\tau_{\text{cell}}$  across the previous cell.

The computation of  $\tau$  along a ray is discussed in Sect. 3.1. Different interactions implemented in `RASCAS` are then described in Sect. 3.2. After this overview, we give details of the numerical implementations in `RASCAS` and test them in Sect. 3.3.

### 3.1. Optical depths and determining the next interaction

The total optical depth  $\tau_{\text{tot}}$  through a mixture of gas and dust can be written as

$$\tau_{\text{tot}}(\nu) = \sum_X \sum_{lu}^{\text{species transitions}} \tau_{X,lu}(\nu) + \tau_{\text{dust}}(\nu), \quad (6)$$

where  $\nu$  is the photon frequency in the frame of the gas (and dust) mixture. The first term on the right-hand side is a sum over all transitions, from a lower level  $l$  to an upper level  $u$ , from all atomic or ionic species  $X$  (hereafter scatterers) present in the gas. The computation of these resonant line optical depths is developed in Sect. 3.1.1. The second term is the contribution of dust, discussed in Sect. 3.1.2. We note that `RASCAS` does not require any line to be present in the above sum, and it can also be used to propagate continuum through a dusty medium. We also note that other continuum contributions can be added to this sum, depending on frequency and/or scatterer. For instance, the absorption in the Lyman continuum can be taken into account by adding a term to this sum (e.g. Inoue & Iwata 2008).

#### 3.1.1. Resonant line optical depth

Along a path of length  $\ell$  through gas at temperature  $T$ , the optical depth due to the transition from a lower level  $l$  to an upper level  $u$  of scatterer  $X$  may be written as a function of frequency  $\nu$  in the gas frame as

$$\tau_{X,lu}(\nu) = \int_0^\ell n_{X,l} \sigma_{X,lu}(\nu, T) d\ell. \quad (7)$$

In this expression,  $n_{X,l}$  is the number density of scatterer  $X$  in electronic state  $l$ . For example, because the spontaneous de-excitation time of `H I` is very short, most `H I` in astrophysical media is in the ground state, and  $n_{\text{H I},1} = n_{\text{H I}}$  is typically a very good approximation. The second term in Eq. 7,  $\sigma_{X,lu}(\nu, T)$ , is

the average cross section at frequency  $\nu$  of a population of scatterers  $X$  at temperature  $T$ . This cross section is the convolution of the natural Lorentzian line shape (in each scatterer's frame) with the Maxwellian velocity distribution of scatterers, due to thermal and/or turbulent motions. The mean thermal velocity of scatterers  $X$  is  $v_{\text{th}} = (2k_B T/m_X)^{1/2}$ , where  $k_B$  is Boltzmann's constant and  $m_X$  the mass of  $X$ . We define the Doppler width  $\Delta\nu_D = (v_{\text{th}}/c)\nu_{lu}$ , where  $\nu_{lu}$  is the frequency of the transition and  $c$  the speed of light. The natural line width in units of the Doppler width is  $a = A_{ul}/(4\pi\Delta\nu_D)$ , where  $A_{ul}$  is Einstein's coefficient for spontaneous emission. We can then write the cross section with the usual Hjerting-Voigt function, valid to first order in  $(v/c)$ :

$$\sigma_{X,lu}(\nu, T) = \frac{\sqrt{\pi}e^2 f_{lu}}{m_e c \Delta\nu_D} H(a, x). \quad (8)$$

Here  $e$  and  $m_e$  are the electron's charge and mass, respectively;  $f_{lu}$  is the oscillator strength of the transition; the dimensionless photon frequency  $x = (\nu - \nu_{lu})/\Delta\nu_D$ ; and

$$H(a, x) = \frac{a}{\pi} \int_{-\infty}^{+\infty} \frac{e^{-y^2}}{(y-x)^2 + a^2} dy. \quad (9)$$

This formalism can be used to compute the optical depth due to any line. Only the values for  $\nu_{lu}$ ,  $A_{ul}$ , and  $f_{lu}$  need to be changed for each transition. In Table A.1 we provide atomic data implemented in RASCAS for a selected sample of lines.

### 3.1.2. Dust optical depth

Along a path of length  $\ell$  through a dusty medium, we can write the total dust optical depth (due to both absorption and scattering) as

$$\tau_{\text{dust}}(\nu) = \int_0^\ell n_{\text{dust}} \sigma_{\text{dust}}(\nu) d\ell, \quad (10)$$

where  $n_{\text{dust}}$  and  $\sigma_{\text{dust}}$  are the number density and cross section of dust grains. In RASCAS we follow by default the formulation of Laursen et al. (2009b): we define  $\sigma_{\text{dust}}$  as a cross section per hydrogen atom, and  $n_{\text{dust}}$  as a pseudo number density given by  $n_{\text{dust}} = (n_{\text{HI}} + f_{\text{ion}} n_{\text{HI}}) Z/Z_0$ . Here,  $f_{\text{ion}} \sim 0.01$  is a free parameter describing how much dust is present in ionised gas, and  $Z_0 \sim 0.005$  (0.01) is the mean metallicity of the Small and Large Magellanic Cloud (SMC and LMC, respectively). As did Laursen et al. (2009b), we use the fits of Gnedin et al. (2008) to compute  $\sigma_{\text{dust}}(\nu)$  for either the SMC or LMC models. Thanks to the modular style of RASCAS, it is straightforward to implement alternative formulations for dust opacity should it be required.

### 3.2. Interactions with matter

When an interaction occurs, it may be with a dust grain, with probability  $P_{\text{dust}} = \tau_{\text{dust}}/\tau_{\text{tot}}$ , or the photon packet may be absorbed in line ( $X, lu$ ), with probability  $P_{X,lu} = \tau_{X,lu}/\tau_{\text{tot}}$ . The current version of RASCAS implements three forms of interactions between photons and matter: (1) resonant scattering (e.g. of Lyman- $\alpha$  photons on H I atoms), (2) interactions with dust (either absorption or scattering), and (3) transitions with multiple decay channels (e.g. fluorescent lines of Fe II). We discuss how these are implemented in the following subsections.

#### 3.2.1. Resonant scattering

In the frame of the gas, where particle motions are isotropic, a scattering event will change the incoming frequency  $\nu_{\text{in}}$  and direction of propagation  $\mathbf{k}_{\text{in}}$  of the photon packet into  $\nu_{\text{out}}$  and  $\mathbf{k}_{\text{out}}$ , depending on the scatterer's velocity  $\mathbf{v}_X$  and mass  $m_X$ , so that to first order in  $v/c$

$$\nu_{\text{out}} = \nu_{\text{in}} \frac{1 + (\mathbf{k}_{\text{out}} - \mathbf{k}_{\text{in}}) \cdot \mathbf{v}_X/c}{1 + (1 - \mu) (h\nu_{\text{in}}/m_X c^2)}, \quad (11)$$

where  $\mu = \mathbf{k}_{\text{out}} \cdot \mathbf{k}_{\text{in}}$ . In Eq. 11, the denominator describes the recoil effect (e.g. Tasitsiomi 2006), which is generally small (Adams 1971), while the numerator carries changes of frames assuming coherent scattering in the frame of the scatterer. Without loss of generality, we can choose a coordinate system in which  $\mathbf{k}_{\text{in}} = (1, 0, 0)$ ,  $\mathbf{k}_{\text{out}} = (\mu, \sqrt{1 - \mu^2}, 0)$ , and  $\mathbf{v}_X/v_{\text{th}} = (u_{\parallel}, u_{\perp,1}, u_{\perp,2})$ , where  $u_{\parallel}$  is the normalised velocity component parallel to the incoming direction of propagation. In this coordinate system, the outgoing frequency  $\nu_{\text{out}}$  is a function of  $u_{\parallel}$  and  $u_{\perp,1}$  alone. For each scattering we draw a value of  $u_{\parallel}$  from a Gaussian distribution biased by the prior that the scatterer interacts with a photon packet of frequency  $x_{\text{in}} = (\nu_{\text{in}} - \nu_{ul})/\Delta\nu_D$ :

$$f(u_{\parallel}) = \frac{a}{\pi H(a, x_{\text{in}})} \frac{e^{-u_{\parallel}^2}}{a^2 + (x_{\text{in}} - u_{\parallel})^2}. \quad (12)$$

We then draw a value of  $u_{\perp,1}$  from the unbiased Gaussian velocity distribution of scatterers  $f(u_{\perp}) = e^{-u_{\perp}^2}/\sqrt{\pi}$ .

The incoming and outgoing directions are related through a phase function, and RASCAS implements a number of these functions. For Lyman- $\alpha$ , for example, we generally use two limiting phase functions, depending on the frequency of the photons in the scatterer's frame  $\nu_{\text{scat,in}} = \nu_{\text{in}}(1 - \mathbf{k}_{\text{in}} \cdot \mathbf{v}_X/c)$ , which reproduce the behaviour of scatterings in the core of the line or in its wings. Following Hamilton (1940) and Dijkstra & Loeb (2008), we use the following phase functions:

$$P_{\text{core}}(\mu) = 11/24 + 3\mu^2/24 \quad (13)$$

when  $|\nu_{\text{scat,in}} - \nu_{X,lu}| < 0.2\Delta\nu_D$ , and

$$P_{\text{wing}}(\mu) = 3(1 + \mu^2)/8 \quad (14)$$

(i.e. Rayleigh scattering) otherwise. The transition at  $0.2\Delta\nu_D$  in the scatterer's frame is discussed in Appendix A of Dijkstra & Loeb (2008) and separates resonant and wing scattering events<sup>2</sup>. For transitions other than Lyman- $\alpha$ , we generally assume isotropic phase functions.

In environments with very high H I opacities, Lyman- $\alpha$  photons will scatter many times locally until their frequency shifts enough for them to make a larger spatial step (see e.g. Dijkstra 2014). In order to reduce the computing time used unnecessarily by these many scattering events, core-skipping algorithms can be implemented, with which we can bias the frequency redistribution in order to move the photon to the wing of the line directly (Ahn et al. 2002; Laursen et al. 2009b). We implemented in RASCAS the core-skipping algorithm described in Smith et al. (2015, Sect. 3.2.4). We note that this acceleration scheme is accurate for media without dust, but will lead to a small underestimation of extinction when dust is present (see discussion in Laursen et al. 2009b). We do not use this acceleration in this paper, except in Sect. 5.1.

<sup>2</sup> Although related, this transition is not to be confused with the transition at  $\sim 3.3\Delta\nu_D$  in the frame of the gas which separates the Gaussian core and Lorentzian wing of the absorption profile.

### 3.2.2. Interactions with dust

When a photon packet interacts with a dust grain, it may either be absorbed or scattered with a probability set by the dust albedo  $a_{dust}(\nu)$ . In RASCAS the dust albedo is a free parameter. By default we use  $a_{dust} = 0.32$  (i.e. 32% of the photons are reflected) for Lyman- $\alpha$  (see Li & Draine (2001) for other frequencies).

When a photon packet scatters on a dust grain, we use the Henyey-Greenstein (Henyey & Greenstein 1941; Laursen et al. 2009b) phase function to compute its outgoing direction

$$P_{HG}(\mu) = \frac{1}{2} \frac{1 - g^2}{(1 + g^2 - 2g\mu)^{3/2}}, \quad (15)$$

with  $g$  the asymmetry parameter. As for the dust albedo, this parameter is a function of frequency, and a free parameter in RASCAS (with a default value  $g = 0.73$  for Lyman- $\alpha$ , taken from Li & Draine 2001).

### 3.2.3. Fluorescent lines

A number of transitions of great observational interest originate from ions that have more complex level structures than simple resonant transitions, in the sense that one absorption channel, say from level  $l_1$  to level  $u$ , leads to more than one decay channel, down to levels  $l_1, l_2, \dots$ . We refer to these transitions of type  $ul_2$  as fluorescent, and a few examples are given in Table A.1. RASCAS deals with these lines easily by having one module per absorption channel. The absorption of photon packets is computed exactly as for resonant lines, but re-emission has a probability of being non-resonant according to the following ratio of Einstein coefficients:

$$P_{ul_i} = \frac{A_{ul_i}}{\sum_i A_{ul_i}}. \quad (16)$$

In the case of fluorescent re-emission, RASCAS simply casts a photon with  $\nu_{ul_i}$  in the frame of the scatterer, assuming an isotropic phase function. When the decay channel is resonant, we follow Sect. 3.2.1.

## 3.3. Numerical implementation

### 3.3.1. Phase functions

Following Barnes (2009), the phase functions given in Eqs. 13 and 14 are analytically integrable and invertible. The solution of this cubic polynomial is a function of the form

$$\mu = (A + B)^{1/3} - (A - B)^{1/3} \quad (17)$$

with

$$B_{\text{core}} = 6(2r - 1) \quad \text{and} \quad A_{\text{core}} = \sqrt{B_{\text{core}}^2 + \frac{11^3}{27}}, \quad (18)$$

$$B_{\text{wing}} = (4r - 2) \quad \text{and} \quad A_{\text{wing}} = \sqrt{B_{\text{wing}}^2 + 1}, \quad (19)$$

and  $r$  a univariate between 0 and 1. The Henyey-Greenstein phase function (given in Eq. 15) is also analytically integrable and invertible, so we obtain  $\mu$  values sampling this distribution by drawing univariate  $r$  in  $[0; 1]$  and computing

$$\mu = \frac{1}{2g} \left( 1 + g^2 - \frac{1 - g^2}{1 - g + 2gr} \right). \quad (20)$$

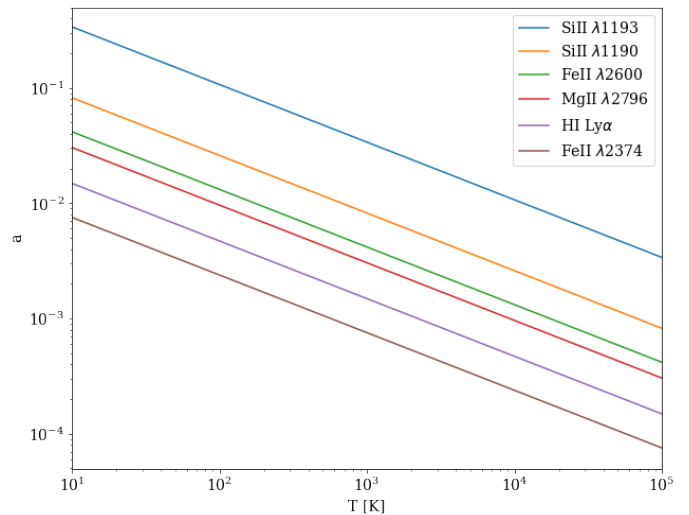


Fig. 1: Voigt parameter ( $a = A_{ul}/(4\pi\Delta\nu_D)$ ) as a function of gas temperature for various species and/or transitions. Some species may not exist in the full temperature range.

### 3.3.2. Voigt function

In Sect. 3.1.1 (Eq. 8), we see that we need to evaluate the Hjerting-Voigt function  $H(a, x)$  in order to compute the line optical depth. There is no analytic solution for this integral, and an accurate numerical integration is computationally expensive. This operation is one of the most frequent in RASCAS, and thus it is essential to use efficient approximations. Unlike most codes, which only focus on the Lyman- $\alpha$  line (e.g. Tasitsiomi 2006; Smith et al. 2015), RASCAS deals with other lines, which have different values, at a given temperature, of the Voigt parameter  $a$ . The normalisation of  $a$ , at a given temperature, is proportional to  $A_{ul}m_X^{1/2}$ . Figure 1 shows  $a-T$  relations for different lines selected from Table A.1. For some transitions, the values of  $a$  can easily be more than one order of magnitude higher than for Lyman- $\alpha$ .

In RASCAS, we implement three different approximations taken from the literature. The simplest approximation we implement is that introduced by Tasitsiomi (2006) in their Eqs. 7 and 8. The second approximation we implement is the more elaborate method by Smith et al. (2015), given in their Appendix A1 (their Eq. A1). The third option is the implementation of the rational form given by Humlíček (1982), which they provide as a Fortran routine (called W4) in the appendix of their paper.

In Fig. 2 we compare the accuracy of these three approximations over a wide range of  $a$  and  $x$  values. We evaluate each method by comparing their predictions to an accurate reference given by the scipy function `wofz3`, which computes the Faddeeva function for complex argument, whose real part is the  $H$  function. It has been shown that this implementation has an accuracy to at least 13 significant digits in both the real and imaginary parts (e.g. Oeftiger et al. 2016). As already shown by Schreier (2011) and Schreier (2017), we find that the Humlíček W4 form is very accurate all over the  $(a, x)$  domain, with a relative error lower than  $10^{-4}$ , as shown by the authors. The approximation given by Tasitsiomi (2006) and widely used for Lyman- $\alpha$  RT in astrophysics (e.g. Verhamme et al. 2006; Semelin et al. 2007; Abe et al. 2018) has an accuracy of around 1% for the Lyman- $\alpha$  line at  $T = 10^4$  K. This accuracy degrades for higher values of  $a$ . In

<sup>3</sup> Steven G. Johnson, Faddeeva W function implementation. <http://ab-initio.mit.edu/Faddeeva>

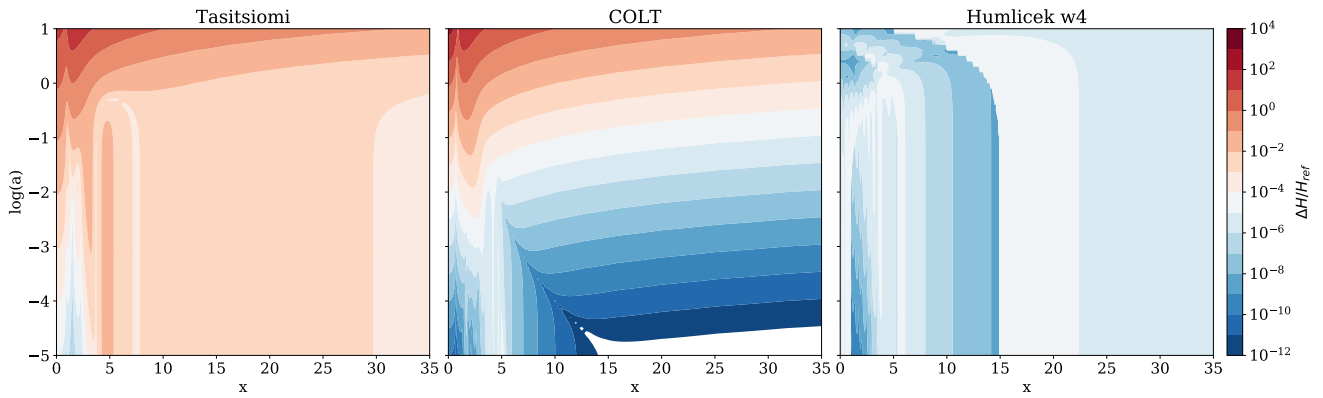


Fig. 2: Contour plot of the relative errors of the three approximations for the Voigt function implemented in RASCAS. *Left*: Approximation from Tasitsiomi (2006). *Middle*: Approximation from Smith et al. (2015). *Right*: W4 approximation from Humlíček (1982). Bluer means more accurate, while redder means less accurate. White parts have a relative error better than  $10^{-12}$ . The transition between light blue and light red is at  $10^{-4}$ .

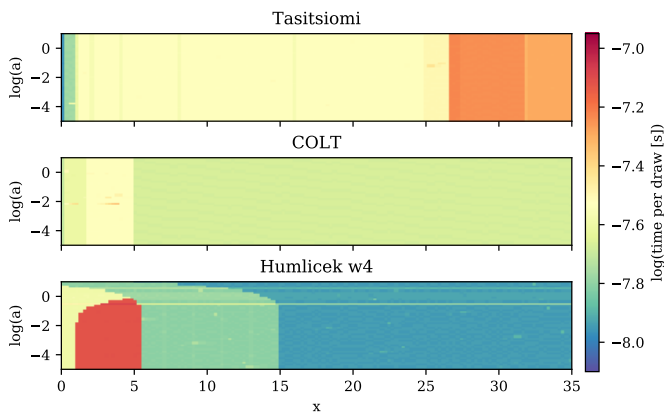


Fig. 3: Measured performance for the computation of the  $H(a, x)$  function in the  $x - \log a$  plane for the three approximations implemented in RASCAS. Colour-coding indicates the log of the time per call in seconds, where bluer indicates faster times.

comparison, the approximation proposed by Smith et al. (2015) has an accuracy lower than  $10^{-4}$  for  $a < 10^{-2.5}$ , i.e. for Lyman- $\alpha$  at  $T > 500$  K. However this approximation gives less accurate results at  $a \geq 10^{-2}$ .

In Fig. 3, we also compare the performance of the three approximations. We time each function by calling it one million times for each point in a grid of values in the  $(\log_{10}(a), x)$  plane, and by measuring the mean CPU time per draw. The top panel shows the timing of the approximation of Tasitsiomi (2006). The fast region below  $x \sim 0.92$  is where the approximation relies only on an exponential. At higher  $x$  values the approximation also requires the evaluation of an extra term, and is thus a bit slower. It is not clear why the method becomes slower at very high values of  $x$ , and this may be tied to uncontrolled compiler behaviours. In the middle panel, the three regions of the approximation of Smith et al. (2015) are clearly visible, even though the CPU time is homogeneous across the full range of values explored here. In the bottom panel, we see clearly the four regions of the method of Humlíček (1982) implemented in the W4 function. The slowest region, at low  $x$  and  $\log a$ , is due to a combination of an exponential function in the complex plane and a

fraction of two polynomial expressions. At  $x > 5$  their method is extremely fast, and is faster than the other methods we tested.

Another way to benchmark the three approximations in order to avoid cache effects and some compiler optimisations is to draw a random distribution of  $x$  values, and to compute  $H(x, a)$  for a fixed value of  $a$ . Here we take  $a = 4.72 \times 10^{-3}$ , which corresponds to  $T = 10^4$  K for the Lyman- $\alpha$  line and we draw  $10^8$  values of  $x$  randomly distributed in the range  $0 < x < 35$ . We find that this takes 3.924s with the Tasitsiomi (2006) approximation, 2.188s with the Smith et al. (2015) approximation, and 2.612s with the Humlíček (1982) approximation.

In conclusion, the three approximations have different behaviours both in terms of accuracy and in terms of computational cost. Choosing one method over another depends on the compromise between performance and accuracy that a problem set requires. The Humlíček (1982) approximation is clearly better than the others in terms of accuracy since it has a  $10^{-4}$  accuracy over a huge range of  $x$  and  $a$ . However, in terms of performance, it depends strongly on the domain of  $x$  and  $a$ , and may be a few times slower than the others at most. On the other hand, the approximation proposed by Smith et al. (2015) appears much more homogenous and seems a bit faster for a long series of computations sampling  $x$  values uniformly. In a typical experiment, however, most draws will happen near  $x \sim 0$ , and the method of Tasitsiomi (2006) may turn out to be faster, though less accurate. We would generally recommend using the method of Humlíček (1982) for metal lines, which may lead to high values of  $a$ . This guarantees a good level of precision and the slight overhead is certainly affordable as metal-line photons do not generally undergo many scatterings. In the case of Lyman- $\alpha$  line transfer, where MCRT is expensive due to the huge number of scatterings that happen preferentially at low  $x$ , the Smith et al. (2015) approximation appears to be a good compromise.

### 3.3.3. Generating $u_{\parallel}$

We implement the rejection method of Zheng & Miralda-Escudé (2002) to sample the distribution of  $u_{\parallel}$  given in Eq. 12. We use the piecewise comparison function:

$$g(u_{\parallel}) \propto \begin{cases} g_1 = 1 / [a^2 + (x - u_{\parallel})^2] & u_{\parallel} \leq u_0 \\ g_2 = e^{-u_{\parallel}^6} / [a^2 + (x - u_{\parallel})^2] & u_{\parallel} > u_0 \end{cases}, \quad (21)$$

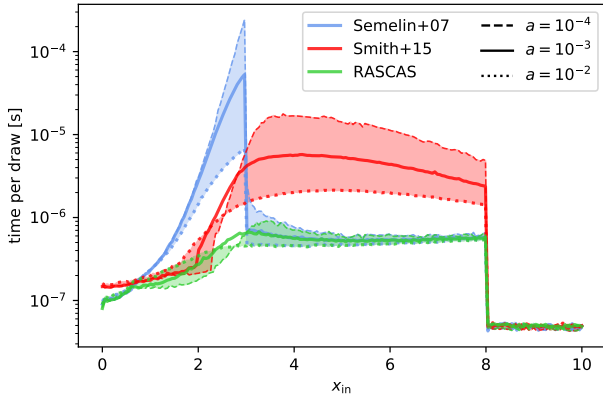


Fig. 4: Measured performance of our draws of  $u_{\parallel}$  in terms of CPU time per draw vs. input frequency  $x_{\text{in}}$ . The methods of Semelin et al. (2007) and Smith et al. (2015) are shown in blue and red, while our approach is shown in green. The solid lines are obtained with  $a = 10^{-3}$ , while the dotted and dashed lines correspond to  $a = 10^{-2}$  and  $a = 10^{-4}$ . The shaded areas indicate the area between these two curves. The non-monotonic behaviour of CPU cost with  $a$  for our method and that of Smith et al. (2015) can be seen: at low  $x_{\text{in}}$ , low  $a$  values are the cheapest, while at high  $x_{\text{in}}$ , low  $a$  values are the most expensive draws.

where  $u_0$  is a separation parameter and the corresponding acceptance fraction is  $\exp(-u_{\parallel}^2)$  for  $g_1$  and  $\exp(u_0^2 - u_{\parallel}^2)$  for  $g_2$ . The efficiency of this method (i.e. the number of rejections) depends heavily on the value of  $u_0$ . Semelin et al. (2007) use an empirical fit (their Eq. 17) at  $x > 3$  and set  $u_0 = 0$  at  $x \leq 3$ . Smith et al. (2015) propose an elegant method used to derive analytic estimates of  $u_0$  for core or wing scatterings (their Eqs. 31 and 32), and effectively set  $u_0 = 0$  at  $x \leq 1$ . Here, we use a 2D polynomial function  $u_0(x, a)$ , which we obtained by empirically finding the  $u_0$  values producing the fastest execution time for a grid of values  $(x, a)$ . This fitting function is the following:

$$\begin{aligned}
u_0 = & 2.648963 + 2.014446\zeta + 0.351479\zeta^2 \\
& + x(-4.058673 - 3.675859\zeta - 0.640003\zeta^2) \\
& + x(3.017395 + 2.117133\zeta + 0.370294\zeta^2) \\
& + x(-0.869789 - 0.565886\zeta - 0.096312\zeta^2) \\
& + x(0.110987 + 0.070103\zeta + 0.011557\zeta^2) \\
& + x(-0.005200 - 0.003240\zeta - 0.000519\zeta^2))\zeta^2, \quad (22)
\end{aligned}$$

where  $\zeta = \log_{10}(a)$ . At high values of  $x$  ( $x \geq 8$  by default), we follow Smith et al. (2015) and directly sample a Gaussian distribution centred at  $1/x$ .

In Fig. 4 we compare the performance of our implementation with those of Semelin et al. (2007) and Smith et al. (2015)<sup>4</sup>. For  $x < 1$ , all methods are equally good, and the results there do not depend much on the value of  $u_0$ . At  $1 < x < 3$ , the method of Smith et al. (2015) improves over that of Semelin et al. (2007) by about an order of magnitude, but the time per draw still drifts up by more than one order of magnitude towards  $x = 3$ . At  $x > 3$ , the method of Semelin et al. (2007) is one or two orders of magnitude faster than that of Smith et al. (2015) depending on the value of  $a$  (low values of  $a$  are slower). At  $x > 8$ , the methods

<sup>4</sup> To be fair, we compare our implementation of Smith et al. (2015), not theirs.

change as we draw  $u_{\parallel}$  from a Gaussian distribution directly. The polynomial function that we implement to decide the value of  $u_0$  as a function of  $(x, a)$  produces results that are always better than or equal to the results of both the Semelin et al. (2007) and Smith et al. (2015) methods.

### 3.4. Test cases

In this section, we present a series of tests that were carried out to validate the MC implementation of the radiative transfer in RASCAS. These tests consist of numerical experiments of single-scattering events and of the full propagation of photons in idealised geometries, for which known analytic solutions exist.

#### 3.4.1. Single-scattering experiments

In Fig. 5 (top panel) we show the frequency redistribution ( $x_{\text{out}}$ ) of Lyman- $\alpha$  photons emitted at various input frequencies ( $x_{\text{in}}$ ) after one scattering on hydrogen atoms. Here we assumed a temperature of 100 K and isotropic angular redistribution ( $W(\theta) = \text{const.}$ ), and we neglected the recoil effect. Our results and the exact redistribution functions derived by Hummer (1962) are nearly indistinguishable. To assess the reliability of the agreement between RASCAS and the Hummer (1962) solution, we plot the relative error between the two ( $\sigma$ ) in units of the relative Poisson error (i.e. the variance due to the limited number of photons per bin in the simulation;  $\sigma_p$ ) in the bottom panel of Fig. 5. We find that the redistribution functions as computed by RASCAS agree almost perfectly with the exact solution, and the tiny differences between the two are due to statistical noise. The overall agreement of RASCAS with the Hummer (1962) solutions confirms the validity of our implementation of the atomic physics for the different transitions available, and of the  $u_{\parallel}$  rejection method used to determine the scatterer's velocity along the propagation of the photons (see Sect. 3.3.3). We show a few additional tests in Appendix B which further validate the implementation of atomic physics in RASCAS.

#### 3.4.2. Idealised configurations

In this section we first compare simulations of Lyman- $\alpha$  RT in idealised static plane-parallel slabs of H I with the analytic solutions of Neufeld (1990) (which are based on the work by Harrington 1973). To derive their solutions, these authors assume that photons scatter mostly in the wings with an absorption Voigt profile approximated as a Lorentzian profile ( $\Phi(x) \approx a/\pi x^2$ ). Their formula are therefore expected to be exact only at very large H I optical depth and low temperature (i.e. in the extremely optically thick regime ( $a\tau_{\text{H I}} \gtrsim 10^3$ )<sup>5</sup>).

In Fig. 6 (left panel) we show the mean number of scatterings of Lyman- $\alpha$  photons ( $x_{\text{in}} = 0$ ) as a function of  $\tau_{\text{H I}}$  for three different slab temperatures ( $T = 10, 10^2, 10^4$  K, or equivalently  $a \approx 0.0149, 0.0047, 0.00047$ ). As expected, we see that our simulations (black points) only reach an excellent agreement with the analytic formula derived by Harrington (1973) (red dashed curve) at low  $T$  and high H I opacities. As shown by Neufeld (1990), the emergent spectrum for the static slab configuration is a double-peak profile centred on  $x_{\text{out}} = 0$ . The middle panel of Fig. 6 shows the spectra computed with RASCAS for various H I opacities (coloured solid curves) assuming  $x_{\text{in}} = 0$  and  $T = 100$  K. Again, our numerical predictions are closer to the

<sup>5</sup> In the following, unless specified otherwise,  $\tau_{\text{H I}}$  stands for  $\tau_{\text{H I, Ly}\alpha}$

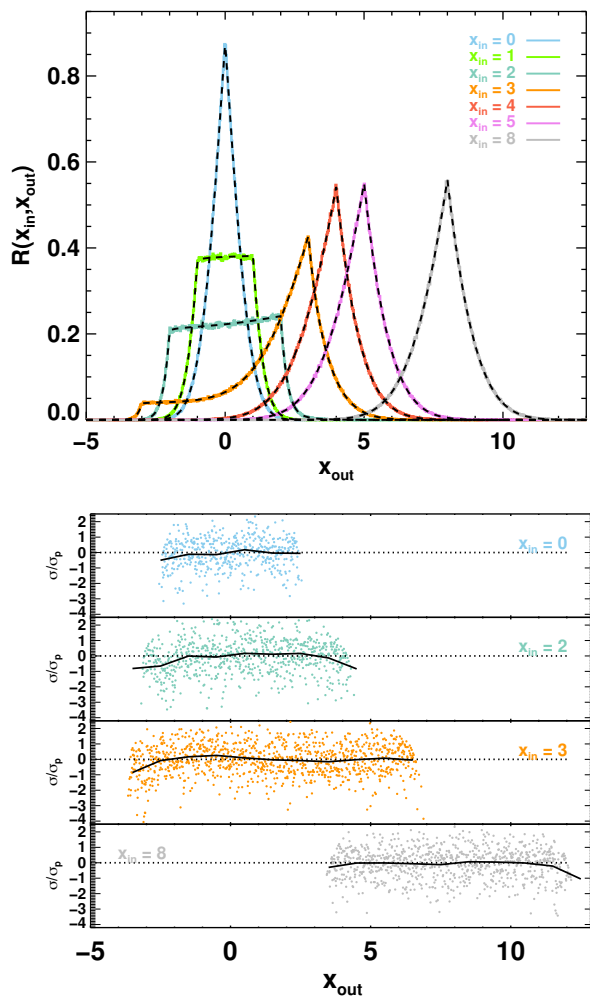


Fig. 5: RASCAS simulations of single-scattering events in a H I medium with  $T = 100$  K assuming isotropic angular redistribution and no recoil effect. *Top*: Frequency redistribution,  $R(x_{\text{in}}, x_{\text{out}})$ , in Doppler units ( $x_{\text{out}}$ ) of Lyman- $\alpha$  photons emitted at  $x_{\text{in}}$  after one single-scattering on a hydrogen atom. The solid coloured curves are the results from RASCAS assuming  $x_{\text{in}} = 0, 1, 2, 3, 4, 5,$  and  $8$ , while the dashed black lines are the analytic solutions of Hummer (1962). *Bottom*: Accuracy of  $R(x_{\text{in}}, x_{\text{out}})$  from RASCAS compared to the solution of Hummer (1962) as a function of  $x_{\text{out}}$ . Here  $\sigma$  is the relative error between  $R(x_{\text{in}}, x_{\text{out}})$  obtained from RASCAS and the solution of Hummer (1962), and  $\sigma_p$  is the relative Poisson error in each bin of  $x_{\text{out}}$  due to the limited number of photons used in this simulation ( $1/\sqrt{N_{\text{phot}}}$ ). In each sub-panel, the solid black curves show the mean value of  $\sigma/\sigma_p$ .

Neufeld (1990) solutions when the medium is optically thicker ( $\tau_{\text{H I}} \gtrsim 10^6$ ).

Finally, using the same framework, Neufeld (1990) investigated the radiative transfer of Lyman- $\alpha$  photons in an absorbing medium and derived an approximated formula for the escape fraction  $f_{\text{esc}}$  of photons through a dusty slab. Because of resonant scattering, the dust attenuation of the Lyman- $\alpha$  line is enhanced and not only depends on the dust opacity  $\tau_{\text{dust}}$ , but also on the H I optical depth  $\tau_{\text{H I}}$  and the gas temperature (via the parameter  $a$ ). The right panel of Fig. 6 shows  $f_{\text{esc}}$  as a function of  $(a\tau_{\text{H I}})^{1/3}\tau_{\text{dust}}$  assuming  $\tau_{\text{H I}} = 10^6$  and  $T = 10^2$  K for several RASCAS runs (black points) compared to the formula of Neufeld (1990) (red

dashed line). We find that the escape fraction decreases in a non-linear fashion as  $\tau_{\text{dust}}$  increases, in good agreement with the analytic prediction.

Various authors have investigated the Lyman- $\alpha$  RT in other simple configurations (Loeb & Rybicki 1999; Dijkstra et al. 2006; Laursen et al. 2009b). In Fig. 7 (top panel), we show the spectra emerging from a uniform static sphere, and compare them with the analytic solution derived by Dijkstra et al. (2006) who used an approach similar to that of Neufeld (1990). Again, we confirm that RASCAS recovers the expected line profile well, especially in the very optically thick regime ( $\tau_{\text{H I}} \gtrsim 10^6$ ). In order to test our code in a non-static experiment, we also perform the simulations of Laursen et al. (2009b) since no analytic solution exists for Lyman- $\alpha$  propagation in moving media. The bottom panel of Fig. 7 shows the spectra for three homogeneous spherical outflow models at  $T = 10^2$  K where the gas velocity increases linearly with radius from 0 to a maximum velocity  $V_{\text{max}}$ . For high outflow velocities ( $V_{\text{max}} = 200, 2000$  km s $^{-1}$ ), the resulting line profiles are asymmetric and are shifted towards negative  $x$  (i.e. longer wavelengths), while for  $V_{\text{max}} = 20$  km s $^{-1}$  a fraction of the photons can escape with positive  $x$  values (i.e. blueward of the line centre). In all cases we see that the agreement between RASCAS (curves) and Laursen et al. (2009b) (crosses) is excellent.

We discuss in Sect. 3.3.2 the systematic errors that arise from various approximations of the Voigt profile. The question arises of how these errors accumulate as a photon performs a random walk in space and frequency. We illustrate this in Fig. 8, where we show the relative differences between the spectra emerging from a static slab illuminated by a central monochromatic Lyman- $\alpha$  source and computed with the different approximations of the Voigt profile. In these experiments the temperature of the gas is set to  $T = 10$  K (i.e.  $a \approx 0.015$ ) so as to maximise the errors (i.e. in the domain of values of  $a$  where the three approximations have different levels of accuracy; see Fig. 2), the opacity of the sphere is  $\tau_{\text{H I}} = 10^7$ , and the number of photon packets is  $10^6$ . In Fig. 8, we show the relative difference between the emerging spectra computed using the approximation from Tasitomi (2006) and that computed using the approximation from Humlíček (1982). This tells us that the two approximations give the same solution at the  $1\sigma$  level. We also did the same comparison for the approximations given by Smith et al. (2015) and Humlíček (1982) and find the same results. This suggests that despite the errors made on one computation of the Voigt function for one value of  $x$  and  $a$  (see Sec. 3.3.2), errors do not accumulate noticeably in experiments with a large number of scatterings.

#### 4. Distributed radiative transfer on adaptive meshes

In a typical RASCAS run, radiation is propagated in structured media defined on adaptive meshes, and within a finite volume. From that viewpoint, Sect. 3 describes what happens within a single simulation cell, and the present section explains how we apply MCRT to a full AMR simulation. One of the main requirements of RASCAS is to limit the memory footprint of the code so that it can be used to process very large simulation outputs on supercomputers with limited RAM per core. This is achieved with (1) domain decomposition (Sect. 4.1), (2) a flexible interface to extract physical quantities from a simulation output (Sect. 4.2), (3) efficient indexing (Sect. 4.3), and (4) a distributed master-worker scheme with optimal adaptive load-balancing (Sect. 4.4).

The three first points above are dealt with in a pre-processing step using the stand-alone code `CreateDomDump`. This code re-

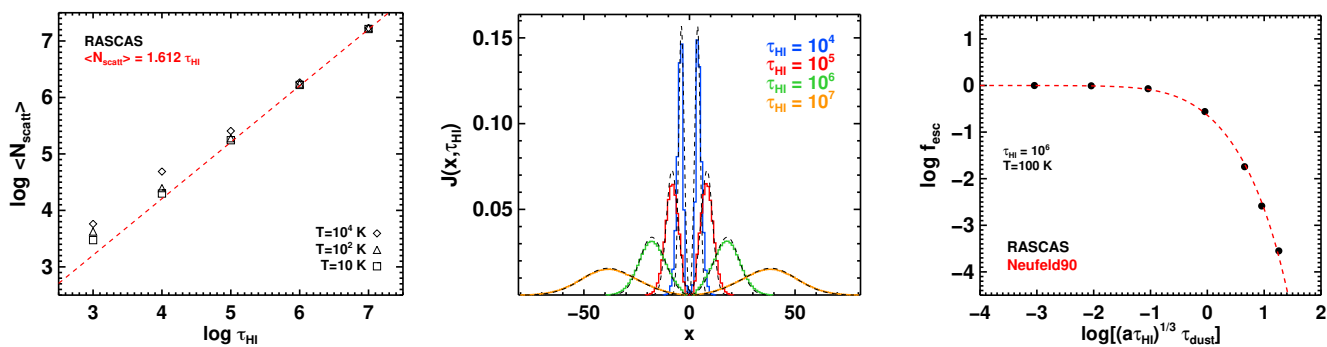


Fig. 6: RASCAS simulations of the transfer of Lyman- $\alpha$  photons ( $x_{\text{in}} = 0$ ) emitted at the origin of a uniform plane-parallel slab. *Left*: Mean number of scatterings until escaping the slab as a function of the vertical H I opacity  $\tau_{\text{HI}}$ . RASCAS runs are shown by black symbols for different assumed gas temperatures ( $T = 10, 10^2, 10^4$  K). The red dashed line corresponds to the analytic approximation found by Harrington (1973),  $N_{\text{scatt}} = 1.612\tau_{\text{HI}}$ . *Middle*: Variation of the emergent spectrum as a function of  $\tau_{\text{HI}}$ . The solid coloured lines are the results from RASCAS, while the black dashed curves are the analytic predictions of Neufeld (1990). We assume  $T = 100$  K, no recoil effect, and an isotropic angular redistribution. *Right*: Evolution of the Lyman- $\alpha$  escape fraction  $f_{\text{esc}}$  as a function of dust optical depth ( $\tau_{\text{dust}}$ ) in the case of a slab with  $\tau_{\text{HI}} = 10^6$  and  $T = 10^2$  K. The results from RASCAS (filled circles) reproduce very well the analytic prediction of Neufeld (1990) (red dashed line).

lies on three RASCAS classes<sup>6</sup> to manage domain decomposition, adaptive mesh indexing, and extraction of physical data from simulation outputs:

- The `domain` class defines the geometric properties of a domain. This class contains public methods which, for example, check whether a point is within a domain or compute the distance of a point to the border of the domain (either the smallest distance or the distance in a given direction). RASCAS implements it for a handful of simple domain shapes, namely spheres, shells, cubes, and slabs<sup>7</sup>, which are defined by a few parameters (their central positions and their size or extent).
- The `gas_composition` class defines the mixture through which radiation propagates (e.g. H I, deuterium, and dust). It implements the conversion of simulation outputs into physical quantities useful for the target RT experiment. This class also manages the interactions of photons with matter. In particular, it contains public methods which return the optical depth along a path and which perform scattering events.
- The `mesh` class handles cells and their indices. The `mesh` class is derived from the `domain` class (i.e. a mesh object is always defined within a domain). A mesh object is built from the collection of (leaf-)cells within its domain. It contains private methods which recompute all necessary indices (see below), and two main public methods which efficiently answer two questions: In which leaf cell is a point? Which neighbouring leaf cell will a photon enter when leaving its current cell with a given direction of propagation? The mesh class is also derived from the `gas_composition` class, so that it can collect and use relevant physical information concerning all leaf cells.

We chose to keep this pre-processing step independent of the MCRT step, in the same spirit as for the casting of photons (see Sect. 2). There are three main reasons. First, this step is not CPU

<sup>6</sup> Although RASCAS is not strictly object oriented, it is very much so in spirit, and we use the object-oriented nomenclature when it improves clarity.

<sup>7</sup> The slab is literally a slice of the simulation box defined only by a thickness in one dimension, and infinite in the two other dimensions thanks to periodic boundary conditions

expensive; on the contrary, it is I/O expensive and possibly requires a lot of memory. Second, it may be necessary to run this code iteratively in order to adjust the free parameters, for instance the parameters of the domain decomposition. Last but not least, it uses the simulation data, so it is best to run this code where the simulation data is stored and then to transfer the relatively light meshes to the computer where MCRT will be computed.

#### 4.1. Domain decomposition

The first domain to define is the computational domain. This is a unique domain which delimits the volume in which the MCRT is done. Photon packets are emitted within this domain and their propagation stops when they reach its border (unless they were absorbed before). This domain has no data directly associated with it.

We then need to cover this computational domain with a series of data domains. Each of these domains defines a mesh object which contains the physical information of all leaf cells within it. The propagation of photon packets through the computational domain is done iteratively through the data domains. When a photon leaves a data domain, it enters the next one, and so on until it leaves the computational domain or is absorbed.

A simple example of domain decomposition is shown in Fig. 9, where two data domains (blue and pink shells) are used to cover the computational domain (sphere outlined with the black circle). The data domains should overlap significantly to minimise photon packets bouncing back and forth between data domains. They should extend slightly beyond the computational domain in order to make sure that all cells intercepted by the computational domain are included in at least one data domain. Using small data domains has two advantages. The first is that the propagation through the mesh should be computationally efficient because it is compact in memory. The second is that each mesh has a controlled and limited size in memory, allowing us to post-process any simulation whatever the RAM of the machine.

We provide a stand-alone code `CreateDomDump`, which can be used to perform domain decomposition for some pre-defined typical geometries. For instance, `CreateDomDump` can produce data domains as a series of concentric shells centred on one

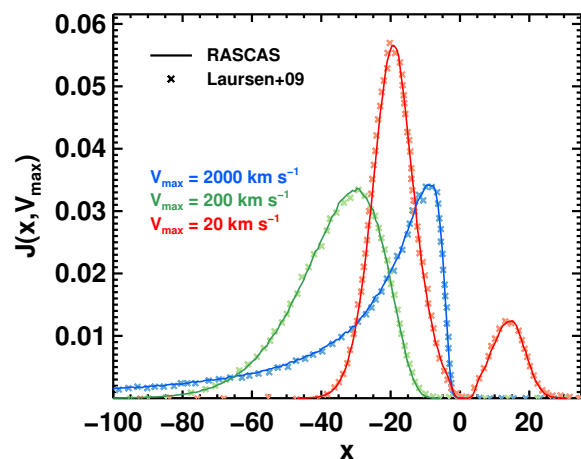
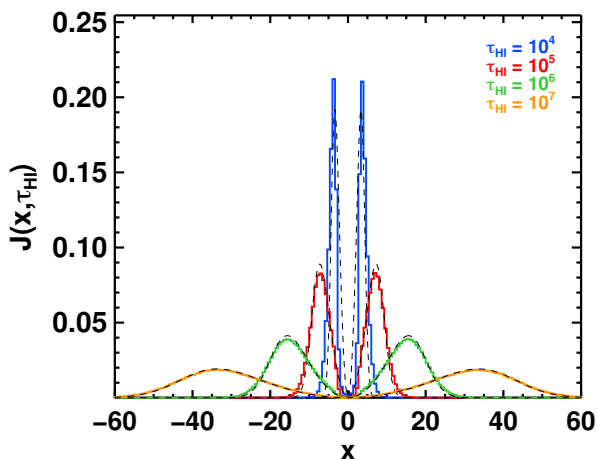


Fig. 7: RASCAS simulations of the transfer of Lyman- $\alpha$  photons ( $x_{\text{in}} = 0$ ) emitted at the centre of a uniform sphere at  $T = 10^2$  K. *Top*: Variation of the emergent spectrum as a function of  $\tau_{\text{HI}}$  for a static sphere. The solid coloured lines are the results from RASCAS, while the black dashed curves are the analytic solutions of Dijkstra et al. (2006). *Bottom*: Non-static sphere with a H I column density of  $2 \times 10^{21} \text{ cm}^{-2}$  in which the gas velocity increases linearly with radius from 0 at the centre to  $V_{\text{max}}$  at the edge of the outflow. The spectra predicted by RASCAS (curves) are compared to Laursen et al. (2009b), who did the same experiments with their code (crosses).

halo (Fig. 9), or as a series of cubes paving a large simulation box. Importantly, the data domains need not correspond to the domains that the simulation code (e.g. RAMSES) has used: `CreateDomDump` will collect the leaf cells belonging to each data domain by searching in all the simulation domains if necessary. There are virtually no constraints here except those cited above: the data domains should cover completely the computational domain, and large overlaps are best when there are multiple scatterings.

Finally, as we discuss in Sec. 4.4, the dynamical load-balancing scheme of RASCAS makes the computational cost of an experiment independent of the domain decomposition. In particular, there is no need to try and define domains that should represent an equal numerical load: RASCAS dynamically adjusts the number of CPUs assigned to each domain so that all processors are active at all times. The main consideration for domain

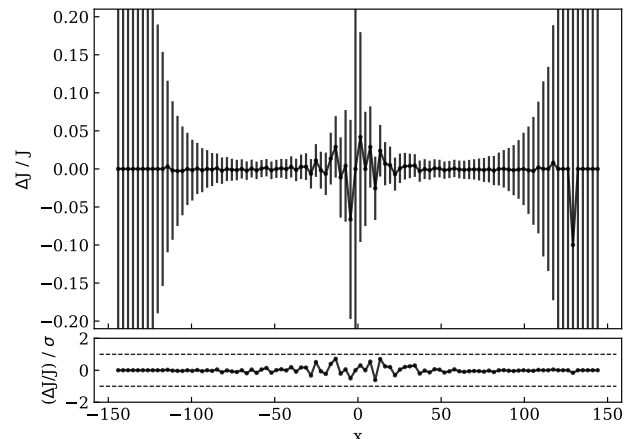


Fig. 8: RASCAS simulations of the transfer of Lyman- $\alpha$  photons ( $x_{\text{in}} = 0$ ) emitted at the origin of a uniform plane-parallel slab with  $\tau_{\text{HI}} = 10^7$  and  $T = 10$  K. *Top*: Relative difference between the emerging spectra computed with the approximation from Tatarski (2006) and that computed with the approximation from Humlíček (1982). *Bottom*: As in the top panel, but in units of the Poisson error (i.e. the variance due to the limited number of photons per bin in frequency;  $\sigma$ ). The horizontal dashed lines show  $\pm 1\sigma$ .

decomposition with RASCAS is thus mainly the memory footprint: no domain should exceed the available RAM.

#### 4.2. Interfaces with simulations

Once data domains are defined, `CreateDomDump` collects leaf cells within each one and defines their physical properties. This is done by the class `gas_composition`. This class needs to be written explicitly by the user following a generic template<sup>8</sup>. This involves three things. First, it needs to define attributes that are necessary for RT through a given gas (and possibly dust) mixture. For example, computing the propagation of Lyman- $\alpha$  photons through hydrogen and dust requires the knowledge of the density of neutral H,  $n_{\text{HI}}$ ; the velocity of the gas,  $v_{\text{cell}}$ ; the thermal velocity dispersion of hydrogen atoms,  $v_{\text{th}}$ ; and the density of dust grains,  $n_{\text{dust}}$ . Second, the class needs to implement a constructor that calls external subroutines to define the values of these attributes for all cells in the domain. In the current version of RASCAS these external subroutines are built for RAMSES (Teyssier 2002) and RAMSES-RT (Rosdahl et al. 2013), and packaged in a single `ramses` module. Such a module may easily be constructed for other simulation codes, and would simply need, in the above example, to contain subroutines that will compute  $n_{\text{HI}}$ ,  $v_{\text{cell}}$ ,  $v_{\text{th}}$ , and  $n_{\text{dust}}$ . Third, the `gas_composition` class implements public methods that return useful quantities such as the optical depth along a given distance, or that perform scattering and/or absorption events. These methods are easily written, as they also rely on external classes that package ion-transition and dust properties. The current implementation of RASCAS provides classes for transitions listed in Table A.1. They represent a vari-

<sup>8</sup> The current version of RASCAS provides a generic template. It also provides implementations for various mixtures of H I, deuterium, and dust, and for some Si II, Mg II, and Fe II fluorescent transitions (see Table A.1). It is straightforward to build new cases from these examples.

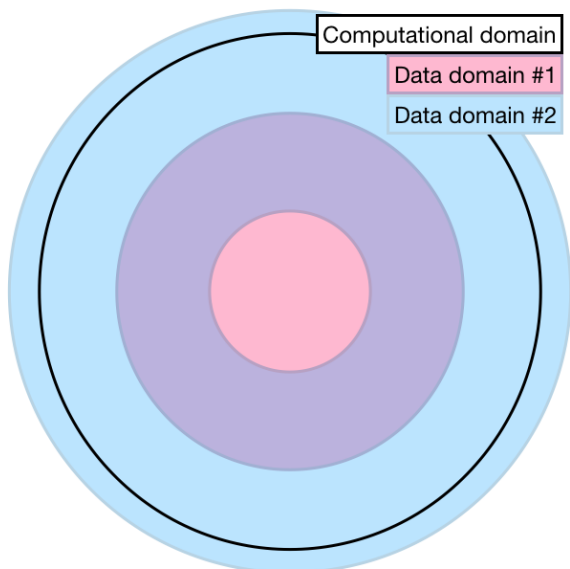


Fig. 9: Example of a domain decomposition with two shell data domains (pink and blue overlapping areas) covering a spherical computational domain (solid black circle). A photon packet emitted from a central source would first propagate through data domain 1 (pink), then be transferred to the data domain 2 (blue), and eventually escape the computational domain. The large overlap between domains 1 and 2 (purple) ensures that the photon is well within domain 2 before being transferred, which reduces possible communication overheads due to photons oscillating between domains.

ety of cases (dust, resonant lines, fluorescent lines) that provide a complete set of examples for future additions, and that can readily be used in custom `gas_composition` implementations.

The second step above is very similar to the `ion_balance` step of `TRIDENT` (see Hummels et al. 2017, Sect. 2.2). Here, we make the slightly different choice to rely on functions that are very closely connected to the simulation code (`RAMSES` in our current implementation) instead of generic functions that, although correct, may not be fully consistent with the assumptions made in the simulation. This choice is also motivated by the fact that we are mostly interested in processing `RAMSES-RT` simulations, which provide the non-equilibrium H I density in all cells directly, accounting for a non-uniform ionising radiation field. This being said, the modular nature of `RASCAS` makes it very easy to plug `ion_balance` or an equivalent into the `gas_composition` class instead of our default `ramses` module.

#### 4.3. Mesh (re-)construction

The final pre-processing step consists in building indices for the leaf cells that fill each domain, so that photon packets can be transported efficiently across the grid. `RASCAS` uses a graded octree structure very similar to that of `RAMSES`, and which requires that two neighbour leaf cells never have more than one level of difference. `RAMSES` meshes satisfy this condition by construction, so any sample of leaf cells from a `RAMSES` simulation output will be useable directly by `RASCAS`. The simplest way to use `RASCAS` to process outputs from other simulation codes (e.g. `SPH`, block-structured AMR, or moving-mesh) would be to convert these outputs to a graded octree structure. For grid-based codes, an

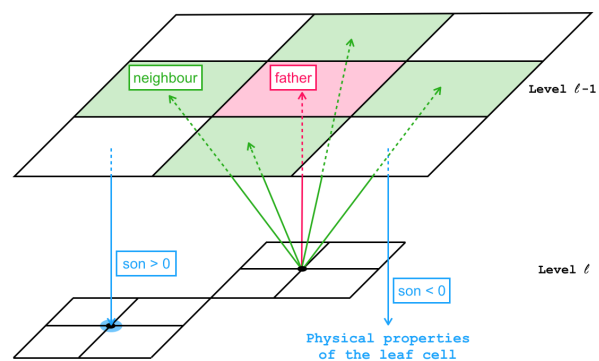


Fig. 10: Two-dimensional illustration of the mesh indexing in `RASCAS`. A level  $l$  oct has five pointers (seven in 3D) to level  $l - 1$  cells: the cell containing the oct (father, red arrow) and the four neighbours (six in 3D) (green arrows). A cell at level  $l - 1$  has a pointer son either to an oct at level  $l$  if it is refined (blue arrow, left) or to the physical properties describing of the cell if it is a leaf cell (i.e. it is not refined; blue arrow, right). See text for a comprehensive description.

alternative would be for the user to provide two routines which (1) efficiently return the index of cell in which a photon packet is located, and (2) efficiently return the neighbour cell into which a photon packet is moving. The modularity of `RASCAS` makes the replacement of these core routines relatively straightforward.

We store the physical properties of the collection of leaf cells in a given domain in flat arrays defined by the `gas_composition` class. These arrays are relatively small as they are reduced to the minimum number of physical properties necessary for the RT computation, and to the number of leaf cells which may be made arbitrarily small with an adapted domain decomposition strategy. We also define an AMR tree structure, which allows us to efficiently locate a leaf cell containing a photon packet or the neighbour leaf cell into which a photon packet is moving. This AMR structure is borrowed from `RAMSES`, and is illustrated in Fig. 10. It consists of three arrays. The father array gives for each oct at level  $l$  the index of the cell at level  $l - 1$  which contains that oct and its eight level  $l$  cells. The neighbour array gives for each oct at level  $l$  the index of the six cells at level  $l - 1$  which are neighbours of the father cell. These two arrays are relatively small as their size is given by the number of octs in the domain. The third array, son, is larger and contains one integer per cell. When the value of son is positive, it is the index of the oct contained in the cell (the inverse of the father link). This is the case when the cell is refined (i.e. when it is not a leaf cell). Such cells are stored solely for search purposes and have no associated physical information. When the value of son is negative, which is the case for leaf cells, then the absolute value of son gives the index of that leaf cell in the arrays which contain the physical properties of all leaf cells. The correspondence between the physical-property arrays and the AMR-tree-structure arrays is thus established with no further variables. The links between the cells of an oct and that oct are defined implicitly through the same indexing convention as in `RAMSES` and also need no further pointers.

It should be noted that we build the mesh and indices with depth-first ordering. This is generally efficient for neighbour searches using the AMR tree, which is important for RT applications. The mesh class features one such routine, which we use abundantly to locate the cells into which photons are entering

after they leave their current cell. This neighbour search works as follows. First, we check whether the escaping photon remains within the father cell (at level  $l - 1$ ) of its current cell (at level  $l$ ). This represents 50% of cases. If so, we walk the AMR tree from there to find the leaf cell into which it is moving (at most two levels). Second, if the photon does not remain in that father cell, there are three neighbour cells (at level  $l - 1$ ) into which it may go, which are on the three faces of the current cell that point outside its father cell. There is again a 50% chance that the photon will enter any of these three cells. We check these cells one by one, and in the case of success, walk the AMR tree from there. Third, it may happen that the two previous searches are unsuccessful because, although very rarely, photons escape diagonally (across vertices or corners of cells). In such a case, testing the many neighbours to determine where photon is might be relatively expensive. Instead, we search for the target leaf cell by walking the AMR tree from the root (level  $l = 0$ ).

#### 4.4. Parallelisation scheme

RASCAS also includes a parallelisation scheme using a master-worker scheme. We make use of the Message Passing Interface (MPI) library to communicate between the master and the workers. This is done by defining an MPI-type photon packet. One MPI thread is the master task and all other MPI threads are worker tasks. The master coordinates work with two key ingredients: a photon-packet queue for each data domain, and an adaptive mapping of workers to data domains (see Sect. 4.1).

In practice, our algorithm works as follows. At initialisation, the master first builds data-domain queues with all photon packets depending on their positions: a photon packet is assigned to the data domain that contains it, and if more than one contain it, to the one within which the photon is furthest away from any border. In other words, photon packets are assigned to data domains in which they will travel the most before moving out, thus minimising data domain changes. Second, the master balances the computational load through domain-worker mapping: the number of workers attributed to each data domain is proportional to the number of photon packets in each data-domain queue. When this is done, the master sends a first series of bundles of photon packets, one to each worker, and waits for any worker to send back its processed bundle. Since the computational time to process a bundle of photon packets is not constant, the communications between the master and the workers are asynchronous.

When the master receives a bundle of photon packets back from a worker, it first determines what to do with each photon packet in the bundle. There are three possibilities. First the photon packet may have escaped the computational domain. In that case the RT is done and the master updates the final properties of this photon packet in order to save it to disc at a later time. Second, the photon packet may have left the data domain of the worker, while remaining within the computational domain. In this case, the master finds the new data domain to which the photon packet belongs, and appends it to the corresponding queue. Third, in the case of RT with a dust component, a photon packet may have been absorbed by a dust grain. In this case, as in the first case, the RT is done, and the master only updates the final properties of this photon packet before saving it to disc. The photon packet type carries a status flag which indicates why the computation ended for each photon packet.

After having processed a bundle of photon packets, the master checks that the CPU mapping is still adequate, meaning that the worker that sent back the current bundle is assigned to a data domain that has more than  $N_{\text{bundle}}$  photon packets in

its queue, where  $N_{\text{bundle}}$  is the number of photon packets in a bundle. If this is the case, the worker keeps its current data domain. On the contrary, if the worker's data domain has an empty queue, the worker is assigned to a new data domain. In this case, we choose the data domain  $i$  with the highest ratio  $\delta(i) = (N_{\text{packet}}(i)/N_{\text{bundle}})/N_{\text{worker}}(i)$ , where  $N_{\text{packet}}(i)$  is the number of photon packets in the queue of data domain  $i$ , and  $N_{\text{worker}}(i)$  is the number of workers associated to the data domain  $i$ . Finally, the master prepares a new bundle of photon packets from the queue of data domain  $i$  and sends it to the worker. The sending phase is always done in two steps. First, the master sends a data domain ID to the worker. The worker receiving the data domain ID checks whether it is the data domain already loaded in memory, and if not, loads it. Second, the master sends the bundle of photon packets, which the worker receives and processes.

This parallelisation scheme has the great advantage of implementing an optimal adaptive load-balancing. Although the queues of different data domains are not balanced at all times, the workers are always at work and the number of data domain changes is minimal. This latter feature is important as it limits a small overhead due to I/O. Also, by construction, the computational load of the master is low, and it spends most of its time waiting for communications from the workers. We use blocking communications (the `MPI_Send` and `MPI_Recv` functions), but since the communications are asynchronous and since there is no synchronisation during the run, the time spent by each worker waiting to send or receive data is extremely limited, and so workers spend most of their time in computing.

Finally, it is also worth mentioning that thanks to this parallelisation scheme, we implement domain decomposition at no CPU cost, which allows us to minimise the memory footprint of the code. Each worker has only the mesh and gas composition data for its data domain, whereas the master has only minimal information (shape and extent) for all domains and photon-packet lists. In practice, data domains may be very small (easily less than 100MB) making RASCAS usable on any architecture to process arbitrarily large simulations.

#### 4.5. Basic test and error budget

Here, we perform some basic tests to demonstrate the precision and efficiency of RASCAS when running RT simulations on full mesh. The test experiment is the propagation of photon packets through a homogeneous and static sphere. In order to assess the precision of the code, we impose that scattering events do not change the propagation direction of photons, so that the distance travelled by all photon packets should be exactly the radius of the sphere, at the precision of the code.

In a first series of experiments, our goal was to measure the numerical error due to our treatment of scattering events only. For this, we used a particular set-up in which the sphere is fully included within one simulation cell. We set the density of the medium so that the optical depth from centre to border,  $\tau_{\text{H}_1}$ , takes values  $10^{-10}$ , 10, and  $10^6$ . We cast  $N_p = 10^6$  photons (only  $10^3$  for the experiment with  $\tau_{\text{H}_1} = 10^6$ ) from the centre of the sphere in random directions, and integrated their travel distances. We then compared these distances to the theoretical distance. For the run with  $\tau_{\text{H}_1} = 10^{-10}$ , there is no scattering event, and the integrated distance is exactly equal to the theoretical distance. In other words, the relative error is zero for all photons. For  $\tau_{\text{H}_1} = 10$ , almost all photon packets have scattered a few times, and there is a tiny difference between the integrated distance and the theoretical one. These errors are of the order of  $10^{-15}$ , the me-

dian is zero and 98% of the photon packets have an error between  $-9 \times 10^{-16}$  and  $9 \times 10^{-16}$ . This error is comparable to the numerical precision  $\sim 2 \times 10^{-16}$  of floating point in double precision in Fortran<sup>9</sup>. For  $\tau_{\text{HI}} = 10^6$ , all photon packets have scattered many times (almost one million scattering events), and we observe that the median value of the relative errors remains equal to zero, but the dispersion increases. For 98% of the photon packets, the relative error is between  $-2.5 \times 10^{-13}$  and  $2.5 \times 10^{-13}$ . This error, which increases with the number of scattering events and with  $\tau_{\text{HI}}$ , as expected, is simply due to the inaccuracy in computing a distance as the sum of ever smaller segments. We find that the amplitude of this error remains very low, even in relatively extreme cases, which validates our implementation.

In a second series of experiments, our goal was to measure the numerical error associated with the propagation of photon packets through a grid. Here, we repeated the same experiments as above, but this time with the sphere filling up a regular mesh of  $256^3$  elements. This time, for each of the three values of  $\tau_{\text{HI}}$ , we find that the median value of the relative errors is the same for the three experiments, and is equal to  $\sim 6.7 \times 10^{-14}$ . The dispersion of these relative errors also remains approximately the same: a relative error between  $\sim -3 \times 10^{-14}$  and  $\sim 2 \times 10^{-13}$  for 98% of the photon packets. This error is mostly due to repeated changes of coordinates at each cell crossing, where the position of a photon is converted from a position in the frame of the current cell, in cell-size units, to a position in the global simulation frame, in simulation-size units, and back to a cell position. Empirically we find that this error is roughly proportional to three times the numerical precision (in double precision) times the number of cells crossed. Again, this shows that the amplitude of the errors is very low, and is well below other uncertainties inherent to the numerical implementation of radiative transfer physics (see Sect. 3.3).

We note that we find the same emergent spectrum for the case of the static uniform HI sphere embedded within one cell and the case of the sphere distributed on a  $256^3$  mesh (see Fig. 7). This demonstrates that the relative errors discussed above are indeed very small with respect to the target result.

Finally, we compare the computational time for all the tests discussed above. We find that when there is no scattering (i.e. for very low values of  $\tau_{\text{HI}}$ ) the overhead of the mesh is important and the computational time may be increased by a factor greater than 10. This is expected because there is basically nothing to compute in these cases, and the small overhead due to cell changes will be relatively important. For higher  $\tau_{\text{HI}}$ , the RT computation through the mesh is only  $\sim 10\%$  slower than without the mesh.

#### 4.6. Scaling of the code

In this section, we discuss the scaling of the code with the number of CPUs. We used RASCAS in a realistic set-up by running the following experiment. We propagated  $10^6$  monochromatic Lyman- $\alpha$  photon packets emitted in star-forming regions through the ISM and CGM of an idealised disc galaxy simulation. The gas is composed of HI, D, and dust. Photon packets were propagated until either they escape the virial radius of the dark matter halo or they are absorbed by dust.

We repeated the same experiment for various numbers of CPUs ranging from 32 to 1024. The results are shown in Fig. 11 where the almost perfect scaling of RASCAS can be seen. This series of runs was done with one single data domain. In principle, this is the most favourable configuration, as it limits both the

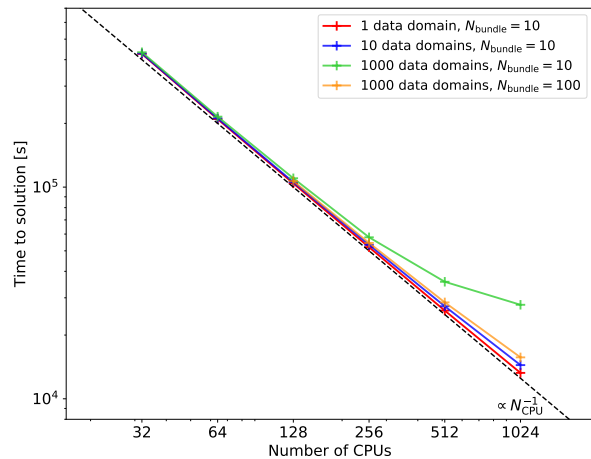


Fig. 11: Scaling test of RASCAS based on an idealised galactic disc simulation: total elapsed time for a realistic MCRT experiment as a function of the number of CPUs used for the run. Red symbols show the results for the series where the computational domain is decomposed into one single data domain, whereas the blue crosses (respectively green crosses) are for the case where the computational domain is decomposed into 10 (resp. 1000) data domains. These three simulations were run with  $N_{\text{bundle}} = 10$ . Orange crosses again show the case where the computational domain is decomposed into 1000 data domains, but this time using  $N_{\text{bundle}} = 100$ . To guide the eye, the dashed line shows the ideal case of relation  $\propto N_{\text{CPU}}^{-1}$ .

amount of communication and the number of times CPUs have to load or unload domains from the disc. However, as discussed in Sec. 4.4, in most cases we expect the efficiency of RASCAS to be independent of the domain decomposition. In order to verify this, we also performed the same test with the computational domain decomposed in 10 (blue symbols) and 1000 (green symbols) data domains. As can be seen in Fig. 11, the total elapsed times for 1 and 10 data domains are very close, confirming our expectations. However, for 1000 data domains the code starts to not scale perfectly for large numbers of CPUs. This is probably due to the very small size of the data domains, which results in photon packets moving from one domain to another after relatively light calculations. This raises the overhead due to communications to a noticeable level which decreases the overall performance.

To confirm this, we performed a profiling analysis of the three runs with  $N_{\text{CPU}} = 512$ . With one data domain, we find that the  $N_{\text{CPU}} - 1$  workers spend most of their time computing ( $> 98\%$ ), whereas the master spends less than 3% computing (i.e. it spends 97% of its time waiting for messages from the workers). It is thus highly available, and the code scales perfectly.

With ten data domains, the number of communications increases by a factor of three compared to the previous case. Then, the  $N_{\text{CPU}} - 1$  workers still spend most of their time computing ( $\sim 95\%$ ), but start to spend  $\sim 5\%$  of their time receiving messages from the master. Since we use blocking communications, and since the sending back of messages to the master of the same amount of data does not cost any time, the workers basically wait for messages from the master because the master has more work to do in managing queues, load-balancing, and sending and re-

<sup>9</sup> This value is given by the intrinsic function `epsilon`, which returns the smallest number  $E$  such that  $1 + E > 1$ .

ceiving messages from the workers. It thus spends  $\sim 9\%$  in computing, decreasing its availability slightly.

With 1000 data domains, the number of communications increases by a factor of nine compared to the case with 10 data domains. The master now spends most of its time computing ( $\sim 60\%$ ), and the workers wait a lot. Their computing times span a broad range from 46% to 92% of their time, with half of them spending less than 75% in computing time. In such extreme cases, the number (and the frequency) of communications is so high that the availability of the master drops completely, resulting in a situation where workers spend from 8% to 54% of their time waiting for messages instead of working.

Fortunately, there is the free parameter  $N_{\text{bundle}}$ , that controls the number of communications. All the computations presented so far have been run with  $N_{\text{bundle}} = 10$ . A profiling analysis of the run with  $N_{\text{CPU}} = 512$  and 1000 data domains, but this time using  $N_{\text{bundle}} = 100$  shows that by increasing the size of the bundle of photon packets sent to each worker, the number of communications drops significantly (by a factor  $\sim 4$ ). Thus, the master has less work and spends 22% of this time computing, increasing significantly its availability. As a consequence, workers wait less and compute more (between 85% and 99%). To confirm that we can recover very good scaling by adjusting the size of the bundle of photons, we performed a series of runs with the computational domain decomposed into 1000 data domains and using  $N_{\text{bundle}} = 100$  (shown with orange crosses in Fig. 11). The total elapsed time is then comparable to the case with one or ten data domains.

In conclusion, we showed that even in the extreme case of 1000 data domains and for large number of CPUs, the overhead by increasing the number of communications can be drastically reduced by increasing  $N_{\text{bundle}}$ . This reduces the number of master-worker communications and then increases the availability of the master. This is one necessary condition that explains why the code scales so nicely with the number of CPUs. Thus, RASCAS can be used with no overhead for an arbitrarily large number of data domains, and it can thus be used to process arbitrarily large simulations even with very limited RAM per core.

## 5. Example applications

In this section we illustrate how RASCAS can be used to construct mock observations which can be directly compared to true observations. It is also worth noting that RASCAS has already been used to compute the radiative pressure due to multiple scattering of Lyman- $\alpha$  photons on hydrogen atoms, and to develop a sub-grid model for early Lyman- $\alpha$  feedback in Kimm et al. (2018). Because of its modularity, RASCAS can also easily be adapted for a number of different applications. For example, its ray-tracing engine has been used to estimate escape fraction of ionising photons from simulated high-redshift galaxies in Trebitsch et al. (2018), Costa et al. (2018), and Rosdahl et al. (2018). Other ‘by-products’ have also been developed to extract and manipulate sub-volumes in large AMR simulations, and to compute column densities along any arbitrary lines of sight.

### 5.1. Lyman- $\alpha$ image of a high-redshift galaxy

The main driver for the development of RASCAS is the study of the Lyman- $\alpha$  properties of galaxies in the high-redshift Universe. In Fig. 12, we show a surface brightness map of Lyman- $\alpha$  emission from a simulated galaxy at redshift  $\sim 4$ . The simulated galaxy has a stellar mass of  $\sim 10^9 M_{\odot}$  and a star formation rate of  $\sim 3 M_{\odot}/\text{yr}$ .

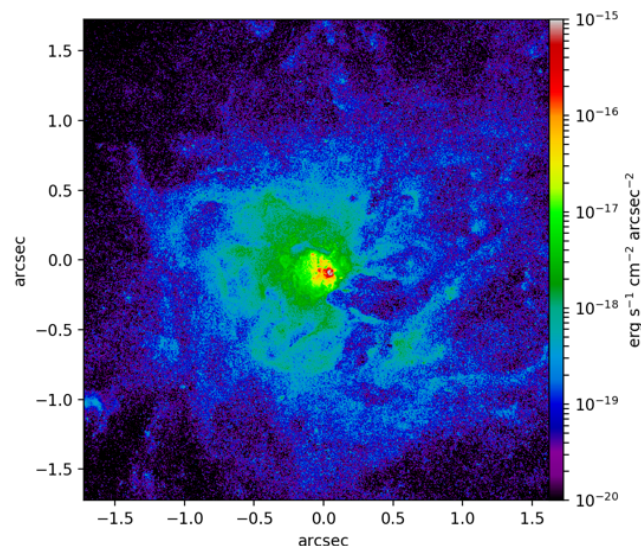


Fig. 12: Surface brightness map of Lyman- $\alpha$  emission from a high-redshift galaxy and its circumgalactic medium.

The simulation and RASCAS post-processing are fully described in Blaizot et al., in prep. It is a radiation-hydrodynamic simulation ran with RAMSES-RT (Rosdahl et al. 2013; Rosdahl & Teyssier 2015; Katz et al. 2017; Rosdahl et al. 2018), with a spatial resolution of  $\sim 15$  pc in the ISM. The sub-grid models used for star formation and feedback are those presented in Kimm et al. (2015, 2017), based on the same calibration as in the SPHINX simulations (Rosdahl et al. 2018).

To construct Fig. 12, we used  $6 \times 10^6$  photon packets, emitted from  $\sim 10^6$  gas cells within the virial radius proportionally to their Lyman- $\alpha$  luminosities, accounting for recombinations and for collisional excitations. We included dust following Laursen et al. (2009b), assuming SMC properties. We used the peeling algorithm (Yusef-Zadeh et al. 1984; Zheng & Miralda-Escudé 2002) as described in Dijkstra (2017, Sect. 9.3) to collect flux on a  $1000 \times 1000$  image in a particular direction. In order to accelerate the computation, we also implemented the core-skipping algorithm described in Smith et al. (2015, Sect. 3.2.4), which slightly underestimates the effect of dust, but produces a speed-up of a factor  $\sim 1000$ .

### 5.2. Line transfer in idealised set-ups

In addition to hydrodynamic simulations, RASCAS can also be run on custom idealised models in which users can decide the sampling and location of the sources as well as the geometry and the properties of the medium. These kinds of set-ups are commonly used to guide the interpretation of observational data (e.g. line profiles) and to test physical scenarios (e.g. inflows and outflows) based on simplified assumptions (e.g. Ahn et al. 2003; Verhamme et al. 2008; Prochaska et al. 2011; Laursen et al. 2013; Scarlata & Panagia 2015). As an illustration, we show in Fig. 13 the output of an RT experiment of a flat UV continuum ( $\lambda = 2570 - 2640 \text{ \AA}$ ) in a galactic wind. In this example, photon packets are emitted at the centre of a spherical expanding outflow that extends from  $r_{\text{min}} = 1$  to  $r_{\text{max}} = 20$  kpc. The medium is filled with Fe II ions distributed according to a given velocity profile ( $v(r) \propto r$ ) and density profile ( $\rho(r) \propto r^{-3}$ ).

The top panel of Fig. 13 depicts the resulting spectrum in which the various features of the UV1 multiplet of Fe II are visible (black line). Strong absorption lines arise at the location of the Fe II  $\lambda\lambda 2586, 2600$  resonant transitions. We note that these two lines are slightly blueshifted due to the bulk motion of the gas, whereas the broadening of the absorption is primarily driven by the velocity dispersion and the column density of the gas. We see that scattering in the outflowing medium gives rise to an emission redward of the  $\lambda\lambda 2586, 2600$  resonances. The other three emission lines at  $\lambda \approx 2612, 2626$ , and  $2632 \text{ \AA}$  correspond to the fluorescent channels associated with the resonant transitions (see Sect. 3.2.1). In our example the convolution of the spectrum with a Gaussian line spread function (overlaid in red), mimicking a typical instrumental spectral smoothing, erases the P Cygni-like features close to the resonances which then appear as pure absorption lines.

Photons emitted by a central source can also resonantly scatter in physical space giving rise to spatially extended emission that traces the surrounding gas. This is shown in the bottom right panel, which represents a mock projected map of the emission of the radiation emerging from the outflow. In the bottom left panel of Fig. 13 we plot the surface brightness profile of the emission at  $\lambda = 2570 - 2640 \text{ \AA}$  (black curve). The emission is strongly peaked at  $r = 0$  because a large fraction of the photons are far away from the resonance and therefore escape directly without scattering (in green). Depending on the opacity of the medium, photons undergoing more than one scattering can contribute significantly to the total surface brightness profile, as is the case in our example in Fig. 13 (coloured dashed lines). This highlights the importance of taking multiple scatterings into account while modelling the radiative transfer of resonant lines, and therefore the need of performing MC numerical simulations, in order to construct mock observables. Finally, we note that  $5 \times 10^6$  photon packets were cast from the source and propagated through the wind until escape of the medium in this simulation, and that it ran on a single core in a few minutes only.

### 5.3. RGB maps of stars with dust from cosmological simulations

RASCAS can also easily be used to compute radiative transfer of continuum light in the presence of dust, and then to produce realistic mock images. As an illustration, we show in Fig. 14 an example of *James Webb* Space Telescope (JWST) NIRCcam images. We note, contrary to dedicated dust MCRT codes (e.g. Jonsson 2006; Baes et al. 2011; Robitaille 2011; Steinacker et al. 2013), that we did not include any modelling of the dust re-emission or of the change in dust temperature (and properties).

We used the radiation-hydrodynamics SPHINX simulations (Rosdahl et al. 2018), the S10\_512\_BINARY run in practise. We extracted from the output at  $z = 6$  a spherical data domain centred onto the most massive halo and with a radius equal to  $1.1R_{\text{vir}}$ . This galaxy has a stellar mass of  $\sim 1.5 \times 10^9 M_{\odot}$  and a star formation rate of  $\sim 5 M_{\odot}/\text{yr}$ . For the `gas_composition` we used the default values for the dust composition (SMC model,  $f_{\text{ion}} = 0.01$ ,  $Z_{\text{ref}} = 0.005$ ).

For the emission of photons, we used the `PhotonsFromStars` spatial sampling and the tabulated continuum from stellar populations for the spectral sampling. To be consistent with the ionising radiative transfer made during the course of the simulation, we used the stellar library by Eldridge et al. (2017). The emitted rest-frame spectrum was decomposed into different parts corresponding to the different photometric

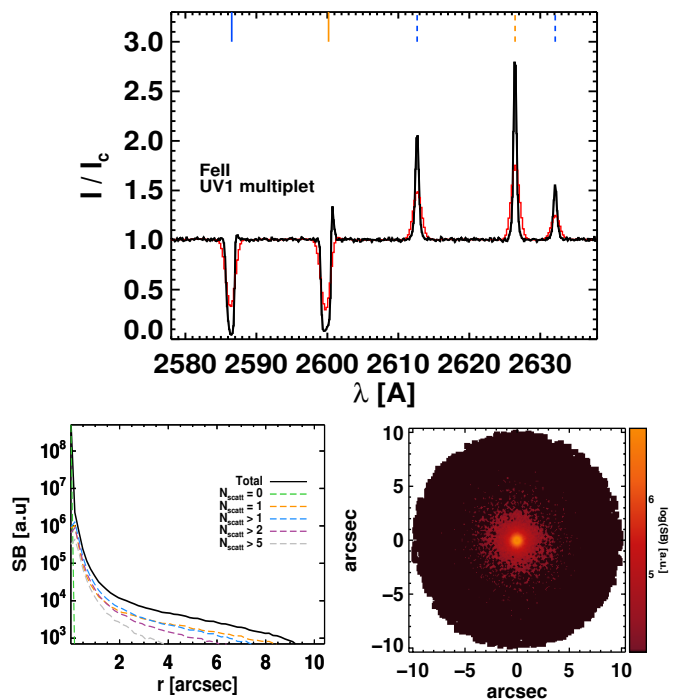


Fig. 13: Simulation of the radiative transfer of the Fe II UV1 multiplet. As input source we cast a flat UV continuum ( $\lambda = 2570 - 2640 \text{ \AA}$ ) propagated through a galactic wind. In our idealised model the gas velocity ( $v(r) \propto r$ ) increases from 0 to  $100 \text{ km s}^{-1}$  and the density profile is described by a power law ( $\rho(r) \propto r^{-3}$ ) normalised to an integrated Fe II column density of  $10^{17} \text{ cm}^{-2}$ . The Doppler parameter, accounting for thermal turbulent motions, is set to  $b = 30 \text{ km s}^{-1}$ . *Top*: Emergent spectrum of the Fe II UV1 multiplet composed of two absorption features and three emission lines (black line). The vertical solid lines show the rest-frame wavelengths of the two resonant transitions ( $2586, 2600 \text{ \AA}$ ), while the dashed lines show the three associated fluorescent emission lines ( $\approx 2612, 2626$ , and  $2632 \text{ \AA}$ ). The red curve shows the Gaussian smoothed spectrum assuming  $FWHM = 1.2 \text{ \AA}$ . *Bottom*: Projected image colour-coded by surface brightness (right) and radial surface brightness profile (left) at  $\lambda = 2570 - 2640 \text{ \AA}$  (in arbitrary units). The total surface brightness profile is represented by the solid black line, and the coloured dashed lines correspond to photons that scattered 0, 1, > 1, > 2, and > 5 times. The image of the extended emission (right panel) has been convolved with a Gaussian assuming a PSF full width at half maximum of  $0.1''$ .

filters of the JWST/NIRCcam, namely F115W, F150W, F200W, F277W, F356W, and F444W. Each wavelength range was sampled with ten million photon packets. We propagated only stellar continuum photons, not the contribution of the nebular emission lines from H II regions.

We computed the dust continuum RT using for each filter a constant value for the albedo  $a_{\text{dust}}$  and the  $g$  parameter according to Li & Draine (2001, Table 6). We again used the peeling algorithm to collect flux into a 3D cube, which is eventually integrated along the spectral dimension using the throughputs of various NIRCcam filters<sup>10</sup> to obtain images. We then dimmed the image using the luminosity distance of the galaxy (at  $z = 6$ ).

<sup>10</sup> <https://jwst-docs.stsci.edu/display/JTI/NIRCcam+Filters>

In Fig. 14, we show a pseudo-colour image combining F150W, F277W, and F444W images at a very high resolution. The effect of dust can be seen with the dust lane in the edge-on view (bottom panel). We also show mock images in the F150W and F444W filters with a noise distribution at a level corresponding to a time exposure of 1 Ms. The two rows show two different projections of the same object. The bottom row is the same projection as in the maps of Rosdahl et al. (2018, Fig. 4).

## 6. Summary and conclusions

In this paper, we have presented a new public 3D Monte Carlo code called RASCAS to compute radiative transfer of resonant lines in simulations of astrophysical objects. RASCAS is written in modern Fortran. The main features of RASCAS are the following:

1. RASCAS computes radiative transport of resonant-line photons through complex mixes of species (e.g. H I, Si II, Mg II) and dust. Although it is designed to accurately describe resonant scattering, RASCAS may also be used to propagate photons at any wavelength (e.g. stellar continuum or fluorescent lines).
2. RASCAS performs RT on an adaptive mesh with an octree structure very similar to that used and produced by RAMSES. With very little effort, RASCAS can be extended to use any (irregular) mesh structure.
3. RASCAS can be easily used to perform RT experiments through idealised gas distributions (e.g. expanding shells, discs) instead of simulations.
4. RASCAS includes tools which allow the user to sample different sources of radiation. In the current distribution, these include a code to spawn photon packets from star particles, taking into account their ages and metallicities and using various SED libraries, and a code to spawn Lyman- $\alpha$  photons emitted by the gas, taking into account both recombination and collisional contributions. RASCAS also features a simple code to produce ad hoc sources which may be used for tests or idealised models.
5. The default outputs of RASCAS are lists of photon packets collected when they escape the computational domain. These are typically analysed through a python class that is provided in the distribution.
6. RASCAS also features a standard peeling algorithm which allows the user to construct mock observations in the form of spectra, images, or datacubes on-the-fly.
7. The modularity of RASCAS makes it very easy to implement new transitions and to compute RT through new mixtures of scatterers and dust. It also makes RASCAS a powerful toolbox to analyse AMR simulations in general. For example, it has been used to compute escape fractions from galaxies of the SPHINX simulations (Rosdahl et al. 2018) by casting hundreds of rays from each star particle in the simulation and integrating the optical depths to ionising radiation along these rays up to the virial radii of host halos.
8. RASCAS is parallelised using MPI and shows perfect scaling at least up to a thousand cores. It also features domain decomposition, which reduces its memory footprint to arbitrarily low values. These features make it usable to process simulations of arbitrarily large sizes on large supercomputers.
9. RASCAS has been fully tested against RT problems with analytic solutions and against various test cases proposed in the literature. In all cases, the agreement between RASCAS and published results is very good.

10. The RASCAS code is publicly available<sup>11</sup>. Future developments of the code will be released and documented at the same URL. RASCAS has been designed to be both easy to use and easy to develop, and we hope to share future developments with a growing community.

*Acknowledgements.* The authors are happy to acknowledge useful and stimulating discussions with H. Katz, C. Scarlata, J. Prochaska, A. Henry, A. Smith, M. Haehnelt, L. Barnes. We further kindly thank B. Sémelin for providing us with parts of his own Lyman- $\alpha$  RT code. We thank J. Rosdahl and V. Mauerhofer for their valuable contributions to improving the code. We acknowledge development of some of the metal-line modules from intern students J. Dumoulin, C. Dubois, A. Collard. We also acknowledge Franz Schreiber for making publicly available his python code for comparing approximations of the Voigt function. We thank the anonymous referee for her/his careful and constructive report.

JB acknowledge support from the ORAGE project from the Agence Nationale de la Recherche under grant ANR-14-CE33-0016-03. TG is grateful to the LABEX Lyon Institute of Origins (ANR-10-LABX-0066) of the Université de Lyon for its financial support within the program “Investissements d’Avenir” (ANR-11-IDEX-0007) of the French government operated by the National Research Agency (ANR). AV acknowledges support from the MHV-SNF grants PP00P2\_1176808, PMPDP2\_175707, and from the European Research Council under grant agreement ERC-stg-757258 (TRIPLE). TK was supported in part by the National Research Foundation of Korea (No. 2017R1A5A1070354 and No. 2018036146) and in part by the Yonsei University Future-leading Research Initiative (RMS2-2018-22-0183). MT acknowledges funding from the European Research Council under the European Community’s Seventh Framework Programme (FP7/2007-2013 Grant Agreement no. 614199, project ‘BLACK’). The development and tests of RASCAS were greatly facilitated by our access to computing resources at the Common Computing Facility (CCF) of the LABEX Lyon Institute of Origins (ANR-10-LABX-0066), and at the CC-IN2P3 Computing Centre (Lyon/Villeurbanne - France), a partnership between CNRS/IN2P3 and CEA/DSM/Irfu.

## References

- Abe, M., Suzuki, H., Hasegawa, K., et al. 2018, MNRAS, 476, 2664  
 Adams, T. F. 1971, ApJ, 168, 575  
 Ahn, S.-H., Lee, H.-W., & Lee, H. M. 2001, ApJ, 554, 604  
 Ahn, S.-H., Lee, H.-W., & Lee, H. M. 2002, ApJ, 567, 922  
 Ahn, S.-H., Lee, H.-W., & Lee, H. M. 2003, MNRAS, 340, 863  
 Bacon, R., Accardo, M., Adjali, L., et al. 2010, in Proc. SPIE, Vol. 7735, Ground-based and Airborne Instrumentation for Astronomy III, 773508  
 Baes, M., Verstappen, J., De Looze, I., et al. 2011, ApJS, 196, 22  
 Barnes, L. 2009, PhD thesis, Institute of Astronomy, Wolfson College, University of Cambridge  
 Barnes, L. A. & Haehnelt, M. G. 2010, MNRAS, 403, 870  
 Barrow, K. S. S., Wise, J. H., Norman, M. L., O’Shea, B. W., & Xu, H. 2017, MNRAS, 469, 4863  
 Behrens, C. & Braun, H. 2014, A&A, 572, A74  
 Behrens, C. & Niemeyer, J. 2013, A&A, 556, A5  
 Bruzual, G. & Charlot, S. 2003, MNRAS, 344, 1000  
 Cantalupo, S., Porciani, C., & Lilly, S. J. 2008, ApJ, 672, 48  
 Cantalupo, S., Porciani, C., Lilly, S. J., & Miniati, F. 2005, ApJ, 628, 61  
 Chisholm, J., Orlitová, I., Schaerer, D., et al. 2017, A&A, 605, A67  
 Costa, T., Rosdahl, J., Sijacki, D., & Haehnelt, M. G. 2018, MNRAS, 479, 2079  
 Dijkstra, M. 2014, PASA, 31, e040  
 Dijkstra, M. 2017, arXiv:1704.03416 [astro-ph], arXiv: 1704.03416  
 Dijkstra, M., Haiman, Z., & Spaans, M. 2006, ApJ, 649, 14  
 Dijkstra, M. & Loeb, A. 2008, MNRAS, 386, 492  
 Drake, A. B., Garel, T., Wisotzki, L., et al. 2017, A&A, 608, A6  
 Eide, M. B., Gronke, M., Dijkstra, M., & Hayes, M. 2018, ApJ, 856, 156  
 Eldridge, J. J., Stanway, E. R., Xiao, L., et al. 2017, PASA, 34, e058  
 Feltre, A., Bacon, R., Tresse, L., et al. 2018, A&A, 617, A62  
 Ferland, G. J., Porter, R. L., van Hoof, P. A. M., et al. 2013, Rev. Mexicana Astron. Astrofis., 49, 137  
 Finley, H., Bouché, N., Contini, T., et al. 2017a, A&A, 605, A118  
 Finley, H., Bouché, N., Contini, T., et al. 2017b, A&A, 608, A7  
 Forero-Romero, J. E., Yepes, G., Gottlöber, S., et al. 2011, MNRAS, 415, 3666  
 Gnedin, N. Y., Kravtsov, A. V., & Chen, H.-W. 2008, ApJ, 672, 765  
 Goerdt, T., Dekel, A., Sternberg, A., et al. 2010, MNRAS, 407, 613  
 Gronke, M. & Bird, S. 2017, ApJ, 835, 207  
 Gronke, M. & Dijkstra, M. 2016, ApJ, 826, 14  
 Hamilton, D. R. 1940, Physical Review, 58, 122  
 Hansen, M. & Oh, S. P. 2006, MNRAS, 367, 979

<sup>11</sup> <http://rascas.univ-lyon1.fr>

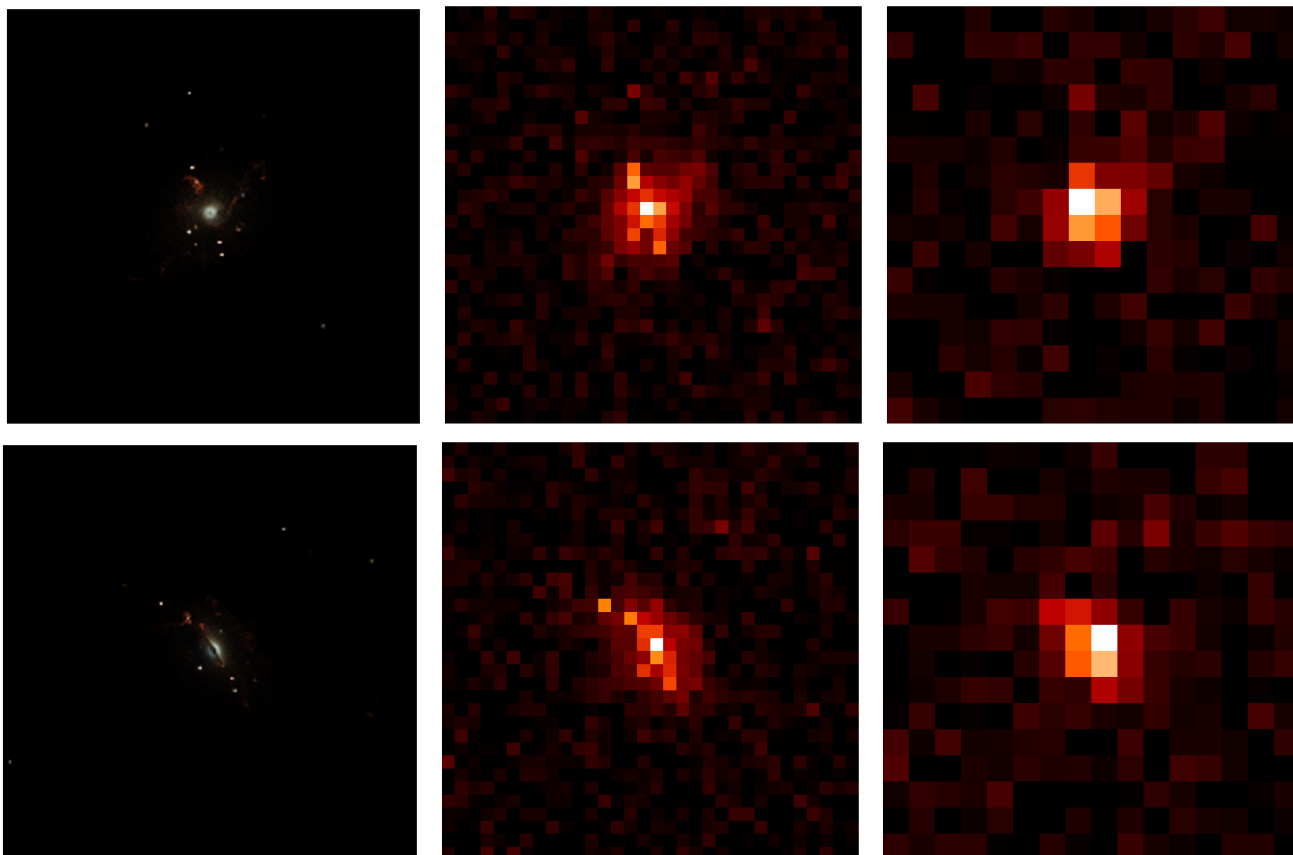


Fig. 14: Mock JWST/NIRCam images. The top and bottom panels show two different projections of the same object. *Left*: Pseudo-colour RGB image with R=F444W, G=F277W, B=F150W. *Middle*: Mock image in the F150W filter at the resolution of JWST/NIRCam in the short-wavelength channel. The noise level corresponds to 1Ms exposure time. Colour-coding indicates the flux level in units of  $\text{erg/s/cm}^2$ . *Right*: Same, but for the F444W filter in the long-wavelength channel. The field of view is the same for each panel ( $\sim 1$  arcsec  $\sim 5.8$  kpc).

- Harrington, J. P. 1973, MNRAS, 162, 43  
 Hashimoto, T., Garel, T., Guiderdoni, B., et al. 2017, A&A, 608, A10  
 Hayes, M., Östlin, G., Schaerer, D., et al. 2013, ApJ, 765, L27  
 Henry, A., Berg, D. A., Scarlata, C., Verhamme, A., & Erb, D. 2018, ApJ, 855, 96  
 Henry, A., Scarlata, C., Martin, C. L., & Erb, D. 2015, ApJ, 809, 19  
 Henyey, L. G. & Greenstein, J. L. 1941, ApJ, 93, 70  
 Herenz, E. C., Wisotzki, L., Saust, R., et al. 2019, A&A, 621, A107  
 Hui, L. & Gnedin, N. Y. 1997, MNRAS, 292, 27  
 Humlíček, J. 1982, J. Quant. Spectr. Rad. Transf., 27, 437  
 Hummels, C. B., Smith, B. D., & Silvia, D. W. 2017, ApJ, 847, 59  
 Hummer, D. G. 1962, MNRAS, 125, 21  
 Inoue, A. K. & Iwata, I. 2008, MNRAS, 387, 1681  
 Itoh, R., Ouchi, M., Zhang, H., et al. 2018, ApJ, 867, 46  
 Jonsson, P. 2006, MNRAS, 372, 2  
 Katz, H., Kimm, T., Sijacki, D., & Haehnelt, M. G. 2017, MNRAS, 468, 4831  
 Kimm, T., Cen, R., Devriendt, J., Dubois, Y., & Slyz, A. 2015, MNRAS, 451, 2900  
 Kimm, T., Haehnelt, M., Blaizot, J., et al. 2018, MNRAS, 475, 4617  
 Kimm, T., Katz, H., Haehnelt, M., et al. 2017, MNRAS, 466, 4826  
 Kollmeier, J. A., Zheng, Z., Davé, R., et al. 2010, ApJ, 708, 1048  
 Kramida, A., Yu, Ralchenko, Reader, J., & and NIST ASD Team. 2018, NIST Atomic Spectra Database (ver. 5.6.1), [Online]. Available: <https://physics.nist.gov/asd> [2018, December 4]. National Institute of Standards and Technology, Gaithersburg, MD.  
 Lake, E., Zheng, Z., Cen, R., et al. 2015, ApJ, 806, 46  
 Laursen, P., Duval, F., & Östlin, G. 2013, ApJ, 766, 124  
 Laursen, P., Razoumov, A. O., & Sommer-Larsen, J. 2009a, ApJ, 696, 853  
 Laursen, P., Sommer-Larsen, J., & Andersen, A. C. 2009b, ApJ, 704, 1640  
 Laursen, P., Sommer-Larsen, J., & Razoumov, A. O. 2011, ApJ, 728, 52  
 Leclercq, F., Bacon, R., Wisotzki, L., et al. 2017, A&A, 608, A8  
 Li, A. & Draine, B. T. 2001, ApJ, 554, 778  
 Li, Y., Hopkins, P. F., Hernquist, L., et al. 2008, ApJ, 678, 41  
 Loeb, A. & Rybicki, G. B. 1999, ApJ, 524, 527  
 Martin-Alvarez, S., Devriendt, J., Slyz, A., & Teyssier, R. 2018, MNRAS, 479, 3343  
 Momose, R., Ouchi, M., Nakajima, K., et al. 2014, MNRAS, 442, 110  
 Neufeld, D. A. 1990, ApJ, 350, 216  
 Oeftiger, A., Aviral, A., De Maria, R., et al. 2016 (JACOW, Geneva, Switzerland), 3090–3093  
 Orsi, A., Lacey, C. G., & Baugh, C. M. 2012, MNRAS, 425, 87  
 Ouchi, M., Shimasaku, K., Akiyama, M., et al. 2008, ApJS, 176, 301  
 Ouchi, M., Shimasaku, K., Furusawa, H., et al. 2010, ApJ, 723, 869  
 Pierleoni, M., Maselli, A., & Ciardi, B. 2009, MNRAS, 393, 872  
 Prochaska, J. X., Kasen, D., & Rubin, K. 2011, ApJ, 734, 24  
 Rivera-Thorsen, T. E., Hayes, M., Östlin, G., et al. 2015, ApJ, 805, 14  
 Robitaille, T. P. 2011, A&A, 536, A79  
 Rosdahl, J., Blaizot, J., Aubert, D., Stranex, T., & Teyssier, R. 2013, MNRAS, 436, 2188  
 Rosdahl, J., Katz, H., Blaizot, J., et al. 2018, MNRAS, 479, 994  
 Rosdahl, J. & Teyssier, R. 2015, MNRAS, 449, 4380  
 Scarlata, C. & Panagia, N. 2015, ApJ, 801, 43  
 Schreier, F. 2011, J. Quant. Spectr. Rad. Transf., 112, 1010  
 Schreier, F. 2017, J. Quant. Spectr. Rad. Transf., 187, 44  
 Semelin, B., Combes, F., & Baek, S. 2007, A&A, 474, 365  
 Shapley, A. E., Steidel, C. C., Pettini, M., & Adelberger, K. L. 2003, ApJ, 588, 65  
 Smith, A., Safranek-Shrader, C., Bromm, V., & Milosavljević, M. 2015, MNRAS, 449, 4336  
 Sobral, D., Matthee, J., Best, P., et al. 2017, MNRAS, 466, 1242  
 Stark, D. P., Ellis, R. S., Charlot, S., et al. 2017, MNRAS, 464, 469  
 Steidel, C. C., Bogosavljević, M., Shapley, A. E., et al. 2011, ApJ, 736, 160  
 Steinacker, J., Baes, M., & Gordon, K. D. 2013, ARA&A, 51, 63  
 Tasitsiomi, A. 2006, ApJ, 645, 792  
 Teyssier, R. 2002, A&A, 385, 337  
 Trainor, R. F., Steidel, C. C., Strom, A. L., & Rudie, G. C. 2015, ApJ, 809, 89

- Trebitsch, M., Verhamme, A., Blaizot, J., & Rosdahl, J. 2016, *A&A*, 593, A122  
Trebitsch, M., Volonteri, M., Dubois, Y., & Madau, P. 2018, *MNRAS*, 478, 5607  
Verhamme, A., Dubois, Y., Blaizot, J., et al. 2012, *A&A*, 546, A111  
Verhamme, A., Orlitová, I., Schaerer, D., et al. 2017, *A&A*, 597, A13  
Verhamme, A., Schaerer, D., Atek, H., & Tapken, C. 2008, *A&A*, 491, 89  
Verhamme, A., Schaerer, D., & Maselli, A. 2006, *A&A*, 460, 397  
Wisotzki, L., Bacon, R., Blaizot, J., et al. 2016, *A&A*, 587, A98  
Yajima, H., Li, Y., Zhu, Q., & Abel, T. 2012, *MNRAS*, 424, 884  
Yang, H., Malhotra, S., Gronke, M., et al. 2017, *ApJ*, 844, 171  
Yusef-Zadeh, F., Morris, M., & White, R. L. 1984, *ApJ*, 278, 186  
Zheng, Z., Cen, R., Trac, H., & Miralda-Escudé, J. 2010, *ApJ*, 716, 574  
Zheng, Z. & Miralda-Escudé, J. 2002, *ApJ*, 578, 33  
Zhu, G. B., Comparat, J., Kneib, J.-P., et al. 2015, *ApJ*, 815, 48  
Zitrin, A., Labbé, I., Belli, S., et al. 2015, *ApJ*, 810, L12

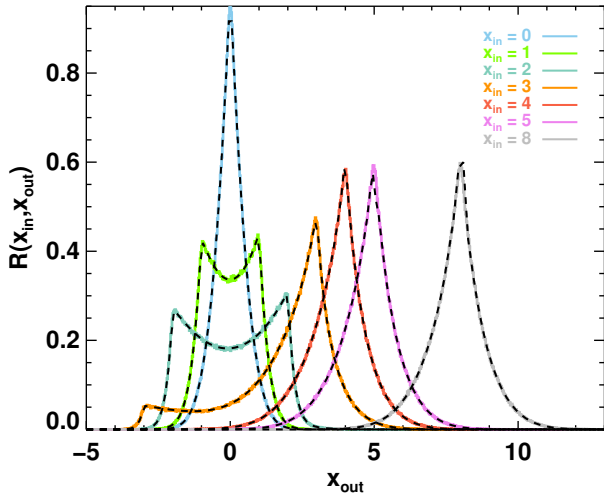


Fig. B.1: Frequency redistribution,  $R(x_{\text{in}}, x_{\text{out}})$ , in Doppler units  $x_{\text{out}}$  of Lyman- $\alpha$  photons emitted at  $x_{\text{in}}$  after one single scattering on a hydrogen atom assuming Rayleigh angular redistribution. The solid coloured curves are the results from RASCAS assuming  $x_{\text{in}} = 0, 1, 2, 3, 4, 5,$  and  $8$ , while the dashed black lines are the analytic solutions of Hummer (1962).

## Appendix A: Atomic data

In Table A.1, we provide atomic data for a selected sample of species and transitions implemented in RASCAS.

## Appendix B: Additional tests

In Sect. 3.4, we present a series of tests based on the comparison of RASCAS with analytic solutions and other MC codes. In Fig. 5, we show the frequency redistribution of Lyman- $\alpha$  photons after one scattering on a hydrogen atom assuming isotropic angular redistribution. Here we repeat the same experiment (Fig. B.1), but we now check the frequency redistribution function for Rayleigh scattering on hydrogen atoms. We find perfect agreement with the expected solution of Hummer (1962).

Figure B.2 compares the mean distance travelled by  $10^6$  Lyman- $\alpha$  photons emitted at  $x_{\text{in}} = 0$  as a function of line-centre opacity  $\tau_{\text{H I}}$  (in black) with the mean free path defined as  $\lambda_{\text{MFP}} = (n_{\text{H I}}\sigma_0)^{-1}$  (red curve), where  $n_{\text{H I}}$  and  $\sigma_0$  are the H I density of the uniform medium and the Lyman- $\alpha$  cross section at line centre for  $T = 100$  K. Again, we confirm that RASCAS recovers well the expected value from the optically thin ( $\tau_{\text{H I}} = 10$ ) to extremely thick regime ( $\tau_{\text{H I}} = 10^8$ ).

RASCAS can also be used to follow radiative transfer through a medium composed of several elements simultaneously. This can be particularly useful if different elements exhibit atomic transitions with comparable energy levels, for example in the case of the Lyman- $\alpha$  line of atomic hydrogen ( $\lambda_{\text{Ly}\alpha} = 1215.67$  Å) and deuterium ( $\lambda_{\text{D,Ly}\alpha} = 1215.34$  Å). In Fig. B.3 we show the spectrum in  $x$  units (normalised to the hydrogen line centre) emerging from a static sphere of H I mixed with deuterium, assuming an abundance of  $\text{D}/\text{H} = 3 \times 10^{-5}$  computed with RASCAS (solid black curve). It can be seen that the presence of deuterium affects the line profile expected for pure H I (i.e. a symmetric double peak; dashed curve in Fig. B.3) by producing a sharp absorption feature in the blue peak of the spectrum at  $x \approx 6.3$ , which

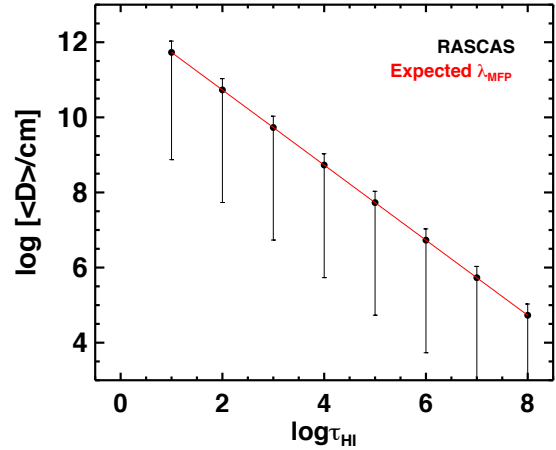


Fig. B.2: Distance travelled by Lyman- $\alpha$  photons emitted at  $x_{\text{in}} = 0$  before their first scattering as a function of H I opacity. The mean travelled distance (filled circles) is in excellent agreement with the expected mean free path ( $\lambda_{\text{MFP}} = (n_{\text{H I}}\sigma_0)^{-1}$ ; red line) at all opacities. Error bars correspond to the  $1\sigma$  standard deviation.

corresponds to the Lyman- $\alpha$  resonance of deuterium. For comparison, we overplot the simulated spectrum of Dijkstra et al. (2006) for the same experiment (blue crosses), and find a very good agreement between the two.

Table A.1: Atomic data for the species and transitions implemented in RASCAS. Each group (between two horizontal lines) shows one absorption line and the decay channel(s) (resonant and fluorescent if any). Data taken from the NIST database (Kramida et al. 2018, <https://www.nist.gov/>).

Species	Transition nickname	Vac. Wavelength (Å)	$A_{ul}$ ( $s^{-1}$ )	$f_{lu}$	Lower Level ( $l$ )	Upper Level ( $u$ )
H	Ly $\alpha$	1215.67	$6.265 \times 10^8$	0.416	1s	2p
D	D Ly $\alpha$	1215.34	$6.265 \times 10^8$	0.416	1s	2p
Si	Si II $\lambda$ 1190	1190.42	$6.53 \times 10^8$	0.277	$3s^2 3p^2 \ ^2P^o \ 1/2$	$3s 3p^2 \ ^2P \ 3/2$
Si	Si II* $\lambda$ 1194	1194.50	$3.45 \times 10^9$	–	$3s^2 3p^2 \ ^2P^o \ 3/2$	$3s 3p^2 \ ^2P \ 3/2$
Si	Si II $\lambda$ 1193	1193.28	$2.69 \times 10^9$	0.575	$3s^2 3p^2 \ ^2P^o \ 1/2$	$3s 3p^2 \ ^2P \ 1/2$
Si	Si II* $\lambda$ 1197	1197.39	$1.40 \times 10^9$	–	$3s^2 3p^2 \ ^2P^o \ 3/2$	$3s 3p^2 \ ^2P \ 1/2$
Si	Si II $\lambda$ 1260	1260.42	$2.57 \times 10^9$	1.22	$3s^2 3p^2 \ ^2P^o \ 1/2$	$3s^2 3d \ ^2D \ 3/2$
Si	Si II* $\lambda$ 1265	1265.02	$4.73 \times 10^8$	–	$3s^2 3p^2 \ ^2P^o \ 3/2$	$3s^2 3d \ ^2D \ 3/2$
Mg	Mg II $\lambda$ 2796	2796.35	$2.60 \times 10^8$	0.608	$2p^6 3s \ ^2S \ 1/2$	$2p^6 3p \ ^2P^o \ 3/2$
Mg	Mg II $\lambda$ 2804	2803.53	$2.57 \times 10^8$	0.303	$2p^6 3s \ ^2S \ 1/2$	$2p^6 3p \ ^2P^o \ 1/2$
Fe	Fe II $\lambda$ 2250	2249.88	$3.00 \times 10^6$	0.00182	$3d^6 4s \ ^6D \ 9/2$	$3d^6 4p \ ^4D^o \ 7/2$
Fe	Fe II* $\lambda$ 2270	2269.52	$4.00 \times 10^5$	–	$3d^6 4s \ ^6D \ 7/2$	$3d^6 4p \ ^4D^o \ 7/2$
Fe	Fe II $\lambda$ 2261	2260.78	$3.18 \times 10^6$	0.00244	$3d^6 4s \ ^6D \ 9/2$	$3d^6 4p \ ^4F^o \ 9/2$
Fe	Fe II* $\lambda$ 2281	2280.62	$4.49 \times 10^6$	–	$3d^6 4s \ ^6D \ 7/2$	$3d^6 4p \ ^4F^o \ 9/2$
Fe	Fe II $\lambda$ 2344	2344.21	$1.73 \times 10^8$	0.114	$3d^6 4s \ ^6D \ 9/2$	$3d^6 4p \ ^6P^o \ 7/2$
Fe	Fe II* $\lambda$ 2366	2365.55	$5.90 \times 10^7$	–	$3d^6 4s \ ^6D \ 7/2$	$3d^6 4p \ ^6P^o \ 7/2$
Fe	Fe II* $\lambda$ 2381	2381.49	$3.10 \times 10^7$	–	$3d^6 4s \ ^6D \ 5/2$	$3d^6 4p \ ^6P^o \ 7/2$
Fe	Fe II $\lambda$ 2374	2374.46	$4.25 \times 10^7$	0.0359	$3d^6 4s \ ^6D \ 9/2$	$3d^6 4p \ ^6F^o \ 9/2$
Fe	Fe II* $\lambda$ 2396	2396.35	$2.59 \times 10^8$	–	$3d^6 4s \ ^6D \ 7/2$	$3d^6 4p \ ^6F^o \ 9/2$
Fe	Fe II $\lambda$ 2383	2382.76	$3.13 \times 10^8$	0.32	$3d^6 4s \ ^6D \ 9/2$	$3d^6 4p \ ^6F^o \ 11/2$
Fe	Fe II $\lambda$ 2587	2586.65	$8.94 \times 10^7$	0.0717	$3d^6 4s \ ^6D \ 9/2$	$3d^6 4p \ ^6D^o \ 7/2$
Fe	Fe II* $\lambda$ 2612	2612.65	$1.20 \times 10^8$	–	$3d^6 4s \ ^6D \ 7/2$	$3d^6 4p \ ^6D^o \ 7/2$
Fe	Fe II* $\lambda$ 2632	2632.11	$6.29 \times 10^7$	–	$3d^6 4s \ ^6D \ 5/2$	$3d^6 4p \ ^6D^o \ 7/2$
Fe	Fe II $\lambda$ 2600	2600.17	$2.35 \times 10^8$	0.239	$3d^6 4s \ ^6D \ 9/2$	$3d^6 4p \ ^6D^o \ 9/2$
Fe	Fe II* $\lambda$ 2626	2626.45	$3.52 \times 10^7$	–	$3d^6 4s \ ^6D \ 7/2$	$3d^6 4p \ ^6D^o \ 9/2$

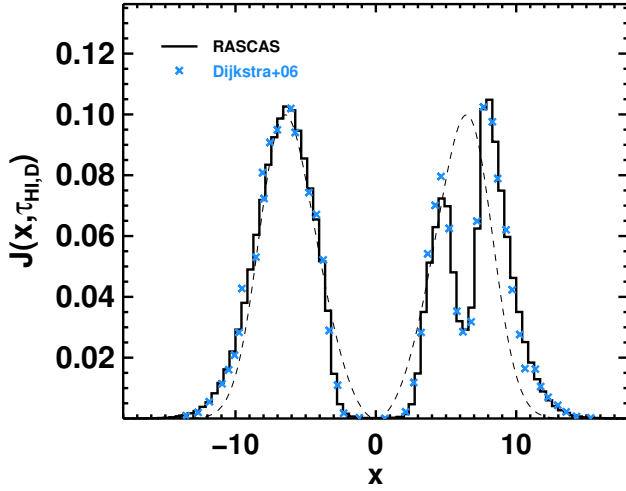


Fig. B.3: Emergent spectrum of Lyman- $\alpha$  photons ( $x_{\text{in}} = 0$ ) emitted at the centre of a uniform static sphere of H I mixed with neutral deuterium D. The model parameters are similar to those used in Figure 3 of Dijkstra et al. (2006):  $T = 10^4$  K,  $N_{\text{H I}} = 2 \times 10^{19} \text{ cm}^{-2}$ , and  $D/H = 3 \times 10^{-5}$ . We recover the same absorption feature as Dijkstra et al. (2006) on the blue side of the Lyman- $\alpha$  line ( $x \approx 6.3$ ), which is due to the presence of deuterium, compared to the case for pure H I (dashed line).